Solid State Communications 389 (2024) 115594

Contents lists available at ScienceDirect

Solid State Communications

journal homepage: www.elsevier.com/locate/ssc

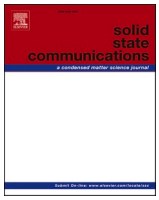

Optimizing the thermoelectric behavior of novel quaternary CoIrMnX (X=Sn, Sb) alloys through chemical potential or carrier concentration doping

T. Ghellab [a,b], Charifi Z [a,b,*], H. Baaziz [a,b,**]

[a] Department of Physics, Faculty of Science, University of M'sila, 28000, M'sila, Algeria
[b] Laboratory of Physics and Chemistry of Materials, University of M'sila, Algeria

ARTICLE INFO

Communicated by: Ursula Wurstbauer

Keywords:
Half-metallicity
Optical response
Spintronic devices
Optoelectronics

ABSTRACT

Materials exhibiting significant polarisation at high spin rates are considered the most promising candidates for spintronic devices. This study investigates the mechanical, optical, spin-polarised electronic structure, magnetism, and thermoelectric properties of CoIrMnX (where X = Sn, Sb). We performed calculations of quaternary Heusler alloys using first-principles calculations. The CoIrMnSn and CoIrMnSb compounds have the most stable Type III crystal structures, according to the calculations performed on the alloys under investigation. We found that the two alloys, CoIrMnSn and CoIrMnSb, possessed a half-metallic ferromagnetic structure, characterised by indirect band gaps of 1.008 eV and 0.806 eV in the predominant spin channels, respectively. Both alloys demonstrate a significant overall magnetic moment of 5 and 6 μβ, respectively. CoIrMnX (where X = Sn, Sb) are ferromagnetic half-metals with 100 percent spin polarisation, according to the results. The results of the elastic constants demonstrate the alloys' mechanical stability. We also investigated optical characteristics such as dielectric function, absorption, reflectance, and optical conductivity. CoIrMnX (where X = Sn and Sb) acts as an efficient absorber in the ultraviolet region and possesses a high refractive index. Alloys exhibit considerable potential as viable candidates for implementation in spintronic devices. The maximum ZT value for CoIrMnSn (CoIrMnSb) is 0.915 (0.6619). To achieve this value, it is necessary to either reduce the charge carrier concentration to $n = 0.0812 \times 10^{20}$ (0.0952×10^{20}) cm^{-3} or the μ to 0.83843 (0.83806) Ryd. Substantially examined materials demonstrate considerable potential for application in the field of thermoelectrics.

1. Introduction

Thermoelectric generators using thermoelectric alloys, which offer sustained power output, have garnered significant interest due to their successful use in spaceship missions over the past two decades. In this study, we aim to investigate the effects of a specific treatment on the participants [1]. The figure of merit, or ZT, calculates the thermoelectric device's energy conversion efficiency based on the Seebeck coefficient S, electrical conductivity σ, absolute temperature T, and the contributions of the lattice k_L and electronic k_e thermal conductivities of the solid materials. These factors are related to each other in the equation: $ZT = \frac{\sigma S^2 T}{(k_L + k_e)}$ [2–4]. Enhancing the power factor, or the figure of merit (ZT), can be accomplished by decreasing the heat conductivity of the material and increasing its electrical conductivity. The achievement of low thermal conductivity (k_L) can be realised by many methods, such as isoelectronic alloying and defect engineering [5–7]. In light of scientific progress and technological advancements, there is a compelling need to develop thermoelectric alloys that possess enhanced electronic and mechanical features. The discovery of a new category of Heusler materials has opened up opportunities for modern technology improvement.

Ternary Heusler (XYZ), full Heusler (X_2YZ), and quaternary Heusler EQH ($XX'YZ$) alloys comprise the majority of Heusler compounds [8]. We produce EQH alloys by substituting an atom of type X′ for one of the X elements in the full Heusler alloys. EQH alloys exhibit comparatively less disorder compared to the ternary Heusler alloy [9]. However, to produce EQH alloys, a lithium ion or another suitable electropositive element fills the appropriate cavities between half Heuslers and full Heuslers, which observe the 24-valence electron rule. They can be easily

* Corresponding author. Department of Physics, Faculty of Science, University of M'sila, 28000, M'sila, Algeria.
** Corresponding author. Department of Physics, Faculty of Science, University of M'sila, 28000, M'sila, Algeria.
E-mail addresses: charifizoulikha@gmail.com, zoulikha.charifi@univ-msila.dz (C. Z), baaziz_hakim@yahoo.fr, hakim.baaziz@univ-msila.dz (H. Baaziz).

https://doi.org/10.1016/j.ssc.2024.115594
Received 13 February 2024; Received in revised form 11 June 2024; Accepted 13 June 2024
Available online 17 June 2024

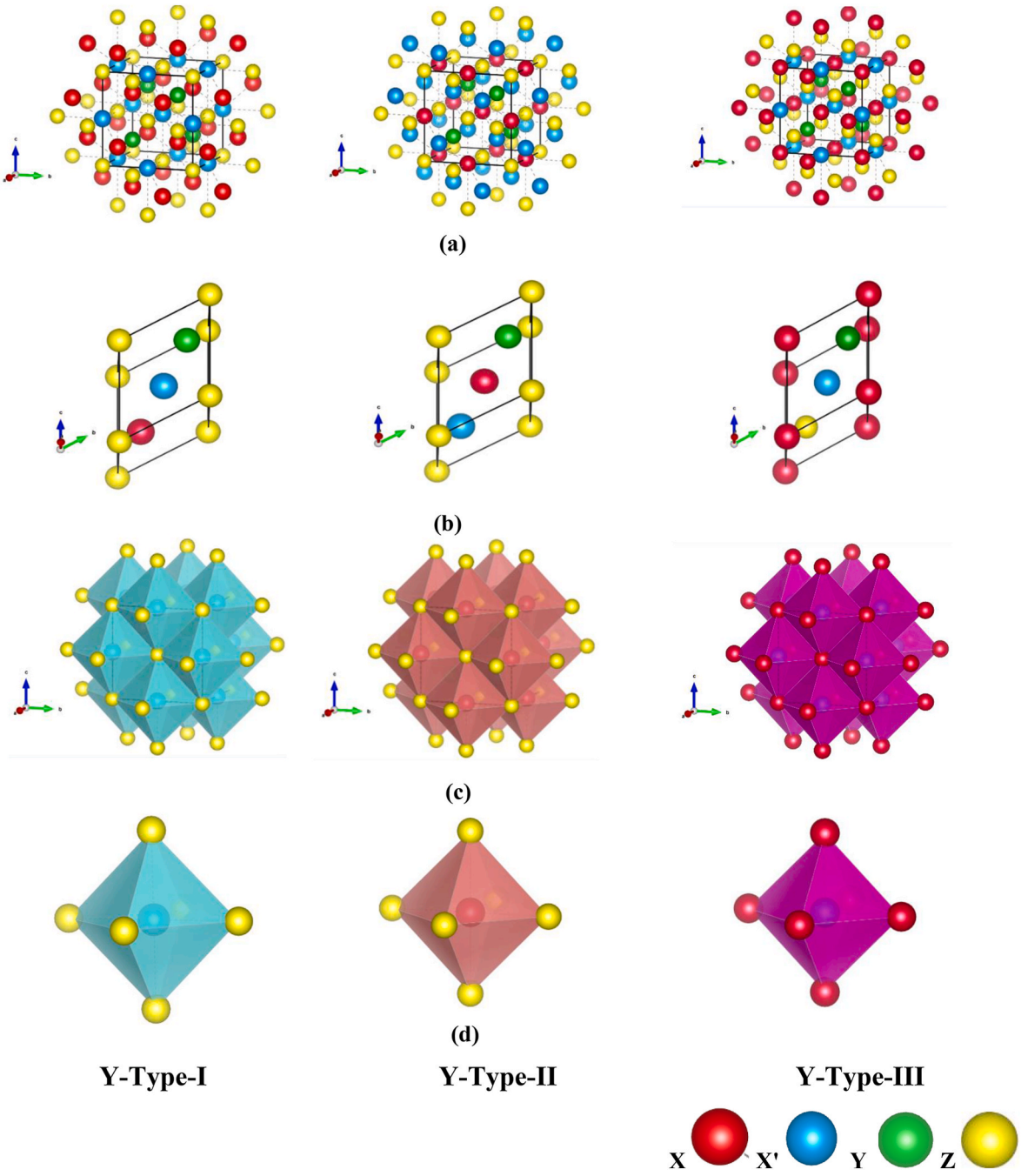

Fig. 1. The three different types of cell **(a)** conventional in the (111) direction, **(b)** primitive in the ($\bar{1}$11) direction, **(c)** octahedral configuration in the (111) direction, and **(d)** X'Z_6, XZ_6, X'X_6 octahedra in the (111) direction of Heusler quaternary compounds X X'YZ.

modified to design a wide range of transport and electronic properties for use in thermoelectric devices, optoelectronics, and other fields. We have undertaken a number of theoretical and experimental investigations in recent years to enhance our understanding of the electronic and thermoelectric properties of these systems [10–14].

Haleoot et al. employed first-principles calculations to examine the remarkable thermoelectric and thermodynamic characteristics of the Quaternary Heusler (QH) compounds CoFeYGe (Y═Ti, Cr) [15]. By utilising density functional theory (DFT), an investigation has been conducted into a recently identified quaternary Heusler compound, CrVNbZn. Notably, it exhibits exceptional electrical and magnetic characteristics, along with a high thermoelectric figure of merit (ZT) of 0.79 throughout a broad temperature range spanning from 260 K to 480 K [16]. Idrissi et al. [17] conducted a study to examine the structural, electronic, and magnetic characteristics of the ZnCdRhMn alloy. This investigation employed first-principles computations and Monte Carlo predictions. Kaur et al. [14] carried out first principles-based calculations for Li-based quaternary compounds, specifically LiHfCoX (where X represents either Ge or Sn). Abraham et al. compared a number of exchange-correlation functions to try to predict the physical and transport properties of LiTiCoSn, a quaternary compound that was just discovered [18]. Gupta et al. examined the ground-state features of the LiScPdPb [19] quaternary Heusler alloy. Singh et al. employed the LiTiCoSn Heusler compound to investigate its mechanical, thermoelectric, and vibrational properties. Plane wave pseudopotential methodology was utilised to conduct the investigation [20].

Table 1
The three different types of crystal structure of quaternary Heusler CoIrMnZ (Z = Sn, Sb) compounds.

Type	4a (0, 0, 0)	4c (1/4, 1/4, 1/4)	4b (1/2, 1/2, 1/2)	4d (3/4, 3/4, 3/4)
Type I	Z=(Sn, Sb)	X=(Co)	X'=(Ir)	Y=(Mn)
Type II	Z=(Sn, Sb)	X'=(Ir)	X=(Co)	Y=(Mn)
Type III	X=(Co)	Z=(Sn, Sb)	X'=(Ir)	Y=(Mn)

The Co-based EQH exhibits a high melting point and conforms to the standard 18 valence electron counts, enabling its potential for the development of thermoelectric devices with high efficiency. Given these underlying motivations, the focus of this research endeavour is limited to the examination of alloys containing cobalt-based EQH CoIrMnX (where X represents either Sn or Sb). The existing literature reveals a dearth of both experimental and theoretical research on these materials. This dearth of examination has served as a catalyst for our decision to undertake studies on them. We conduct the investigation of the structural, electronic, mechanical, optical, and transport properties of the new compounds CoIrMnZ (Z = Sn, Sb) using first-principles calculations in conjunction with BoltzTraP. Section 2 of the present work outlines the calculating process, while Section 3 delves into the discussion of the findings. Ultimately, Section 4 serves as the culmination of the preceding content, presenting the final outcomes and deductions.

2. Computational method

Wien2k, a computational code founded on density-functional theory (DFT) [21], was utilised to acquire the outcomes. In conjunction with the Perdew, Burke, and Ernzerhof Generalized Gradient Approximation (GGA) functional, the structural characteristics were acquired by employing the all-electron full potential linearized augmented plane wave (FP-LAPW) method [22]. The modified Becke Johnson (mBJ) [23], which is presently an industry standard for accuracy in its application, was utilised to evaluate the electronic and optical properties. The mBJ functional improves the accuracy of band gap estimations in comparison to the frequently used LDA/GGA functionals, as supported by empirical evidence [24,25]. The potential being discussed demonstrates autonomy from orbitals and has the capacity to accurately predict the band gap of various compounds, such as semiconductors, and insulators, by virtue of a substantial degree of correlation. Academic sources [24,26] have supported the existence of this occurrence. We limited the plane wave expansion to an energy cutoff of 400 Ryd, and ceased the attenuation of the relative atomic position relaxation when the energy level surpassed 10^{-4} Ryd. The calculations were performed consistently, adhering to convergence criteria of 0.05 mRy/a.u for atomic force and 0.001 e for charge. Convergence is determined by multiplying the smallest radius of the muffin-tin sphere (R.M.T) with the maximum vector of the plane wave (k_{max}). The value of R.M.T $\times$ k_{max} is chosen to be 9. The calculation of optical properties necessitated the use of 20,000 k-points in total. The study employs a plane wave cut-off of $G_{max} = 12$ atomic units (a.u^{-1}) to analyse R.M.T values for the elements Co, Ir, Mn, Sn, and Sb, which range from 2.33 to 2.46 atomic units (a.u). We used a 100,000 k-point to maximize the usefulness of transport parameter research. We can perform the calculation of transport factors for materials using the BolzTrap technique [27], a constant relaxation time approximation (CRTA) was assumed and set to $\tau = 10^{-14}$ s (default τ for BoltzTraP2 code) for all the QHA compounds investigated. The calculation of elastic constants is executed utilising the IRELAST method [28], which is a WIEN2k package component. The Debye temperature (θ_D) and Grüneisen parameter (γ), which are thermodynamic parameters, were ascertained through the utilisation of the Gibbs functions, the quasi-harmonic Debye models, and the Gibbs2 code [29].

2.1. Structural and mechanical description

The quaternary Heusler compounds, exemplified as LiMgPdSb, have a crystalline structure known as the Y-structure, characterised by the space group $F\bar{4}3m$. Theoretically, it is possible for them to form crystals in three distinct non-equivalent superstructures [30,31], as seen in Fig. 1 and Table 1. The complexity of ground state calculations for magnetic materials arises from the presence of several local minima, which are not observed in metals. Therefore, we make the assumption that both paramagnetic and ferromagnetic configurations are considered in order to ascertain the ground state of the materials under investigation, as presented in Fig. 2. We compare the total energies of several configurations to identify the stable structure within the given stoichiometry. Table 2 presents the comparison of total energies, optimised lattice parameter, and total spin magnetic moment of the materials in three distinct non-equivalent superstructures. Ferromagnetic states are shown by Heusler's quaternary materials throughout the range of accessible configurations. The compounds CoIrMnSn, and CoIrMnSb are classified as Type III in this state (see Fig. 2). The optimised lattice's parameters

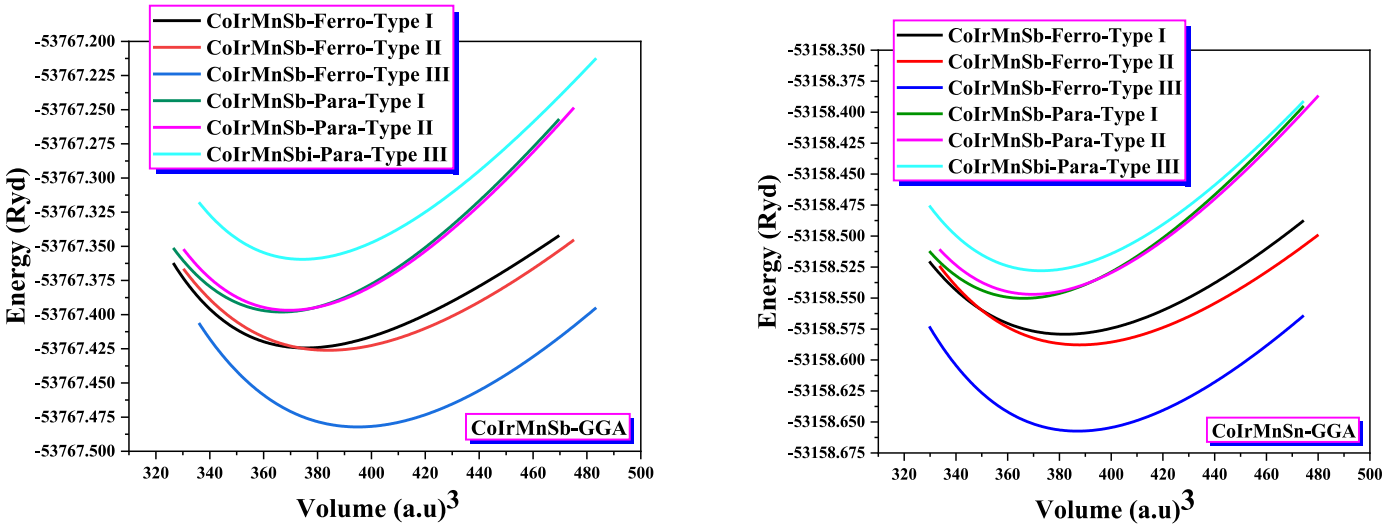

Fig. 2. The variation of energy as a function of volume in the non-magnetic (Paramagnetic) and magnetic (Ferromagnetic) cases for the three types of quaternary Heusler compounds CoIrMnSn and CoIrMnSb.

Table 2
The values of the lattice constant a, the modulus of compressibility B, its derivative B', the volume, and the minimum total energy E_{min} calculated by the GGA approximation of the quaternary Heusler compounds CoIrMnSn, and CoIrMnSb. Here, bold indicates the most stable phase.

Compounds	Type	Physical Parameters	Our calculations		Theoretical calculations [32]
			Para	Ferro	
CoIrMnSn	Type I	a (Å)	6.0109	6.0957	6.1999
		$(\Delta a/a)_{theo}$	−3.14 %	−1,70 %	–
		B (GPa)	240.5856	181.0072	–
		B'	5.0634	4.6159	–
		E_{min} (Ryd)	−53158.550172	−53158.579244	–
		Volume (u.a)^3	366.3944	382.1226	–
		M_{Tot} (μ_B)	–	5.18413	5.21
	Type II	a (Å)	6.0295	6.1262	6.2245
		$(\Delta a/a)_{theo}$	−3.23 %	−1.60 %	–
		B (GPa)	240.2862	181.4222	–
		B'	4.9797	4.9645	–
		E_{min} (Ryd)	−53158.546928	−53158.587832	–
		Volume (u.a)^3	369.8127	387.8857	–
		M_{Tot} (μ_B)	–	5.70580	5.31
	Type III	a (Å)	6.0471	**6.1221**	6.1999
		$(\Delta a/a)_{theo}$	−2.52 %	**−1.27 %**	-
		B (GPa)	236.0169	**209.3945**	-
		B'	5.0320	**5.0715**	-
		E_{min} (Ryd)	−53158.527963	**−53158.657451**	-
		Volume (u.a)^3	373.0598	**387.1044**	-
		M_{Tot} (μ_B)	–	**5.09916**	5.01
CoIrMnSb	Type I	a (Å)	6.0134	6.0631	6.1794
		$(\Delta a/a)_{theo}$	−2.76 %	−1.91 %	–
		B (GPa)	238.7117	187.5372	–
		B'	5.1863	6.9642	–
		E_{min} (Ryd)	−53767.398016	−53767.424489	–
		Volume (u.a)^3	366.8551	376.0234	–
		M_{Tot} (μ_B)	–	5.60518	4.67
	Type II	a (Å)	6.0292	6.1060	6.2033
		$(\Delta a/a)_{theo}$	−2.88 %	−1.59 %	–
		B (GPa)	242.1656	169.0932	–
		B'	5.1793	5.1195	–
		E_{min} (Ryd)	−53767.396768	−53767.426131	–
		Volume (u.a)^3	369.7491	384.0766	–
		M_{Tot} (μ_B)	–	5.74929	4.68
	Type III	a (Å)	6.0558	**6.1637**	6.2390
		$(\Delta a/a)_{theo}$	−3.02 %	**−1.22 %**	–
		B (GPa)	236.1818	**187.2140**	–
		B'	5.4519	**4.4735**	–
		E_{min} (Ryd)	−53767.359414	**−53767.482233**	–
		Volume (u.a)^3	374.6713	**395.0608**	–
		M_{Tot} (μ_B)	–	**5.95729**	6.00

are presented in Table 2, demonstrating strong agreement with previous theoretical studies [32]. The lattice parameter optimisation of the Heusler quaternary compounds CoIrMnZ (where Z represents either Sb or Sn) exhibits a favourable level of concurrence with the theoretical value as proposed by *Nepal* et al. [32]. The compound CoIrMnSn exhibits the highest compressibility module in its ferromagnetic phase, followed by CoIrNNSb. This study represents the first attempt to reveal the energy values associated with the fundamental states V, B_0, and B' of the Heusler quaternary compounds CoIrMnSn and CoIrMnSb. Currently, our understanding of the compressibility module values for these fascinating materials is insufficient. The computation's findings can aid in the initiation of empirical endeavors aimed at characterizing these novel materials.

Cohesive and formation energies can be utilised to determine the physicochemical stability of quaternary CoIrMnX (X = Sn, Sb) Heusler alloys:

$$E_{coh} = \frac{1}{4}\left[E_{Tot}^{CoIrMnX} - \left(E_{atom}^{Co} + E_{atom}^{Ir} + E_{atom}^{Mn} + E_{atom}^{X}\right)\right] \quad (1)$$

$$E_{For} = \frac{1}{4}\left[E_{Tot}^{CoIrMnX} - \left(E_{bulk}^{Co} + E_{bulk}^{Ir} + E_{bulk}^{Mn} + E_{bulk}^{X}\right)\right] \quad (2)$$

where $E_{Tot}^{CoIrMnX}$ is the equilibrium total energy in the most stable phase for CoIrMnX (X = Sn, Sb). E_{atom}^{Co}, E_{atom}^{Ir}, E_{atom}^{Mn}, and E_{atom}^{X} are the isolated atomic energies of the elements Co, Ir, Mn, and X = Sn or Sb, for CoIrMnSn or CoIrMnSb, respectively, E_{bulk}^{Co}, E_{bulk}^{Ir}, E_{bulk}^{Mn}, and E_{bulk}^{X} are the equilibrium total energies per atom for bulk Co, Ir, Mn, and X = Sn or Sb, for CoIrMnSn or CoIrMnSb, respectively. The formation/cohesion energies for CoIrMnSn and CoIrMnSb have been calculated to be −0.23/-6.20 eV/atom, and −0.09/-5.86 eV/atom, respectively. The negative numbers demonstrate the stability and feasibility of these two materials' experimental synthesis. We have calculated the cohesion and formation energies of FeVScSb to be −0.49 eV/atom and −5.07 eV/atom, respectively. For FeVYSb, the values are −0.21 eV/atom and −4.82 eV/atom, respectively. These calculations were also performed for FeNiMnAl, resulting in −0.36 eV/atom and −7.71 eV/atom, and for FeNiMnSi, resulting in −0.31 eV/atom and −8.17 eV/atom [33,34]. Following these findings, we exclusively examined the structure of CoIrMnX (X = Sn, Sb) for its electronic, elastic, and magnetic properties.

The CoIrMnX (X = Sn, Sb) compounds under investigation exhibit a crystalline structure in the cubic phase. Consequently, these compounds contain three distinct second-order elastic constants, specifically C_{11}, C_{12}, and C_{44}. Table 3 presents the computed C_{ij} values for CoIrMnX (where X represents Sn or Sb) using the GGA approximation. The calculated C_{ij} values adhere to the Born-Huang stability criteria [35,36], as stated:

$$C_{11} - C_{12} > 0, C_{11} > 0, C_{44} > 0, C_{11} + 2C_{12} > 0, C_{11} < B < C_{12} \quad (3)$$

Table 3
The elastic parameters, the anisotropy index, the melting temperature T_{melt}, the velocity of both the longitudinal and transverse waves (v_t, v_l), the mean velocity of sound (v_m), and the temperature of Debye Θ_D.of the quaternary Heusler compounds CoIrMnSn, and CoIrMnSb.

	CoIrMnSn-Type III	CoIrMnSb-Type III
C_{11} (GPA)	249.1416	195.064
C_{12} (GPA)	187.6204	171.082
C_{44} (GPA)	139.6760	110.851
B_H (GPA)	208.128	179.075
G_V (GPA)	96.109	71.306
G_R (GPA)	57.805	25.792
G_H (GPA)	76.957	48.549
E_V (GPA)	249.865	188.851
E_R (GPA)	158.720	73.831
E_H (GPA)	205.537	133.575
σ_V	0.299	0.324
σ_R	0.372	0.431
σ_H	0.335	0.375
A_1	4.54074	9.24452
T_{melt} (K)	2025.4268 ± 300	1643.1987 ± 300
B_H/G_H	2.70444	3.68851
A_G %	24.8864	46.8741
A^U	3.31317	8.82323
v_t (m/s)	2501.64	1578.78
v_l (m/s)	5026.87	4326.61
v_m (m/s)	2807.15	1792.85
Θ_D (K)	343.994	218.217

The objective of this research endeavour is to assess the mechanical stability of CoIrMnX (X = Sn, Sb) compounds when in the cubic phase and exposed to ambient conditions. The elastic constants help to assess the mechanical resilience, elasticity, and resistance to deformation forces demonstrated by the compounds under investigation. C_{44} is a measure of a material's resistance to stress-induced deformations, whereas C_{11} quantifies the stiffness of the material when subjected to applied stress [37]. The constant C_{11} exhibits a greater magnitude compared to other constants used in our computations. This observation suggests that the compounds under investigation have a higher degree of resistance to alterations in length as opposed to modifications in shape or volume. The <100> crystallographic direction is anticipated to exhibit the highest density. The compound C_{11} (CoIrMnSn) has superior properties compared to C_{11} (CoIrMnSb). This results in a higher degree of rigidity in CoIrMnSn bonds compared to CoIrMnSb bonds along the [100] direction. The comparison between C_{44} (CoIrMnSn) and C_{44} (CoIrMnSb) suggests that CoIrMnSn exhibits a higher degree of monoclinic shear deformation in the (100) planes along the [010] direction, as compared to CoIrMnSb. Table 3 displays the calculated values of additional elastic constants, including the bulk modulus B, shear modulus (G), Young's modulus (E), Poisson's ratio (σ), and Zener anisotropic factor (A_1), which can be computed as $A_1 = \frac{2C_{44}}{C_{11}-C_{12}}$. Under conditions of absolute zero temperature and pressure, Type III records the determined B values for CoIrMnSn and CoIrMnSb as 208.128 GPa and 179.075 GPa, respectively (see Table 3). The observed outputs closely resemble those obtained from the equation of state, specifically 209.3945 and 187.2140 GPa, as presented in Table 2. We find that CoIrMnSn exhibits more stiffness than CoIrMnSb, as evidenced by its higher shear modulus and Young's modulus. The values obtained for both compounds exhibit a departure from unity, indicating their pronounced anisotropic behaviour [38]. The ductile/brittle and ionic/covalent properties of the studied quaternary CoIrMnX (X = Sn, Sb) Heusler alloys can be judged using Poisson's ratio (σ), Pugh's ratio (B/G), and Cauchy pressure (C_{12}–C_{44}). Compounds with ductile properties typically exhibit Poisson's ratios greater than 0.33 [39]. The spectrum of σ values pertaining to central forces in materials and ionic crystals is commonly observed to be between 0.25 and 0.5 [39]. On the other hand, covalent substances demonstrate σ values that span from 0.1 to 0.25, indicating that interatomic forces are classified as non-central forces [40,41]. It is apparent from the results in Table 3 that the computed values of σ for CoIrMnSn and CoIrMnSb are 0.335 % and 0.3755 %, respectively.

This observation indicates that both materials possess ductility and demonstrates characteristics of central forces and ionic characteristics. Pugh's criterion [42,43] classifies a material as ductile if its Pugh's ratio exceeds 1.75, and classifies materials with a Pugh's ratio below this threshold as non-ductile. Table 3 presents the determined Pugh's ratio values for CoIrMnSn and CoIrMnSb, which are 2.704 and 3.688, respectively. These results provide confirmation of the ductile characteristics exhibited by both alloys. The positive value of Cauchy pressure [44,45] supports the affirmation of these compounds' ductility. We have also calculated the average, transverse, and longitudinal sound velocities of the compounds CoIrMnSn and CoIrMnSb in addition to the aforementioned calculations. The data shown in Table 3 provides proof that elastic longitudinal waves have a higher propagation speed compared to elastic transverse waves. We have computed the Debye temperature (θ_D) based on the given sound velocities.

Many physical characteristics, such as the crystal's specific heat capacity, thermal conductivity, and melting temperature, all relate to its elastic constants through the Debye temperature, a significant physical parameter. The Debye temperature (θ_D) can be determined from the temperature dependence of the second-order elastic constants at low temperatures. It has been seen that CoIrMnSb has a lower Debye temperature (θ_D) than CoIrMnSn. This could mean that the lattice thermal conductivity is lower. The direct correlation between the Debye temperature and lattice thermal conductivity [46] establishes this relationship. We have examined the melting temperature (T_{melt}) of the CoIrMnX (X = Sn, Sb) materials and presented it in Table 3. The existence of crystallographic elastic anisotropy can have a substantial influence on a range of physical phenomena, including but not limited to anisotropic deformation, susceptibility cracking, and elastic instability. The CoIrMnX compound exhibits elastic anisotropy, with X representing either Sn or Sb has been measured utilising three additional distinct methodologies in addition to the initial calculation of the Zener parameter (A_1).

The second approach entails evaluating the degree of elastic anisotropy under shear circumstances, as described in reference [47]:

$$A_G = \frac{(G_V - G_R)}{(G_V + G_R)} \times 100 \quad (4)$$

For isotropic materials, the A_G value is zero. Anisotropy exists in elastic shear between A_G and zero. At one hundred percent A_G, the utmost potential anisotropy is present. The distinction between CoIrMnSn and CoIrMnSb is their shear anisotropy A_G. As shown in Table 3, the corresponding percentages for the values are approximately 24.886 and 46.874, according to the GGA approximation. CoIrMnZ (Z = Sn, Sb) materials demonstrate a notable level of anisotropy with respect to their shear modulus. In comparison to the CoIrMnSn compound, the anisotropic shear modulus of CoIrMnSb is the highest.

The third approach entails the computation of the universally recognised index, sometimes referred to as the universal index [48].

$$A^U = 5\left(\frac{G_V}{G_R}\right) + \frac{B_V}{B_R} - 6 \quad (5)$$

A^U values for isotropic materials are zero. Crystallographic anisotropy undergoes a transition whereby its magnitude changes from zero to positive. We computed the universal index A^U using the GGA approximation for CoIrMnSn and CoIrMnSb in Type III, as demonstrated by the data in Table 3. The A^U values obtained are respectively 3.313 and 8.823, correspondingly. Each compound demonstrates substantial elastic anisotropy.

When considering practical applications, surface structures that display Young's modulus's directional reciprocal are more desirable. The following describes how three-dimensional polar diagrams may be utilised to depict the distribution of the E modulus for a cubic system

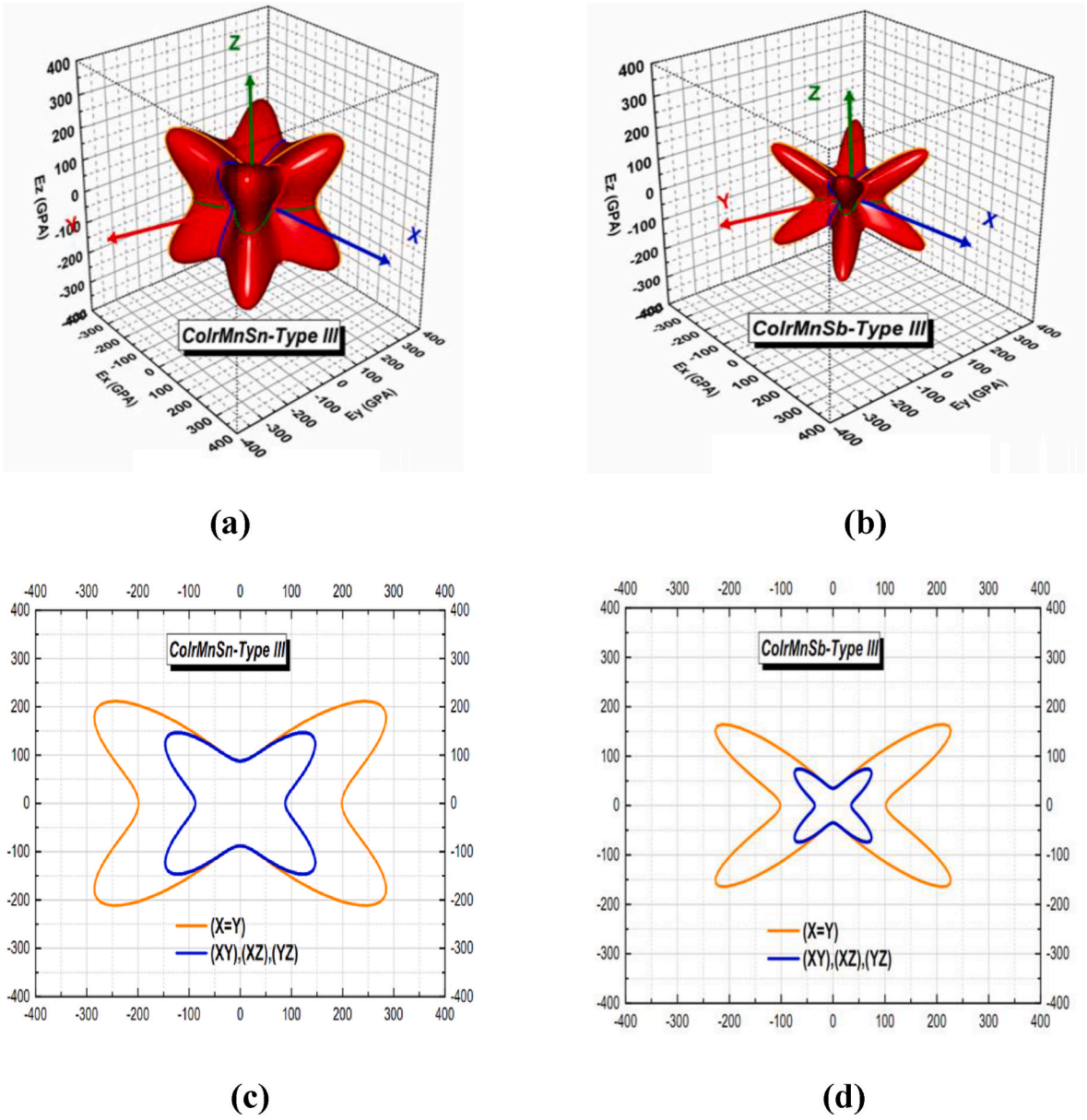

Fig. 3. Graphs of the 3D surface of the Young's modulus **(a)** CoIrMnSn, and **(b)** CoIrMnSb, **(c)**, and **(d)**, their transverse sections in separated planes, respectively.

[49]:

$$E = \frac{1}{S_{11} - 2\left(S_{11} - S_{12} - \frac{1}{2}S_{44}\right)\left(n_1^2 n_2^2 + n_2^2 n_3^2 + n_3^2 n_1^2\right)} \tag{6}$$

Regarding spherical coordinates, the orientations along the x, y, and z axes correspond to the cosine values $n_1 = \sin\theta\cos\varphi, n_2 = \sin\theta\sin\varphi$, and $n_3 = \cos\theta$, where S_{ij} is the deformability elastic constant. Fig. 3 illustrates Young's modulus for CoIrMnZ (Z = Sn, Sb) in relation to the projected orientation, using the elastic compliance coefficients as a reference point. The solution to equation (6) generates a three-dimensional closed surface, where the Young's modulus in the given direction corresponds to the distance between the surface and the origin of the associated coordinate system. This surface would have the appearance of a sphere if the underpinning structure were entirely isotropic. Clearly, according to Young's modulus, the surfaces of CoIrMnZ (where Z = Sn, Sb) do not have a spherical morphology. These two compounds demonstrate a significant degree of anisotropy due to the unique bonding properties possessed by adjacent atomic planes. Consequently, a considerable separation exists among the atomic planes. For the CoIrMnZ (Z = Sn, Sb) materials, the elastic anisotropy is greater in the (X = Y) plane than in the (XY), (XZ), and (YZ) planes. We have observed that the anisotropy of the compound CoIrMnSb is more obvious than the compound CoIrMnSn.

2.2. Electronic and magnetic properties

The electronic structures of the examined CoIrMnX (X = Sn, Sb) compounds are analysed using band structure and density of states plots, with the optimised lattice parameters acquired by the PBE-GGA method in the most stable type. The spin-polarised band structure of Heusler's Type III for quaternary compounds CoIrMnSn and CoIrNSb, was computed along the high symmetry paths of the first *Brillouin zone*. The mBJ-GGA approximation revealed that the two Heusler CoIrMnSn and CoIrMnSb quaternary compounds exhibit semi-metallic (half-metal) behavior, as depicted in Fig. 4. This is due to the fact that the majority spin bands traverse the *Fermi* energy level, indicating metallic characteristics, whereas the structure of the minority spin bands is

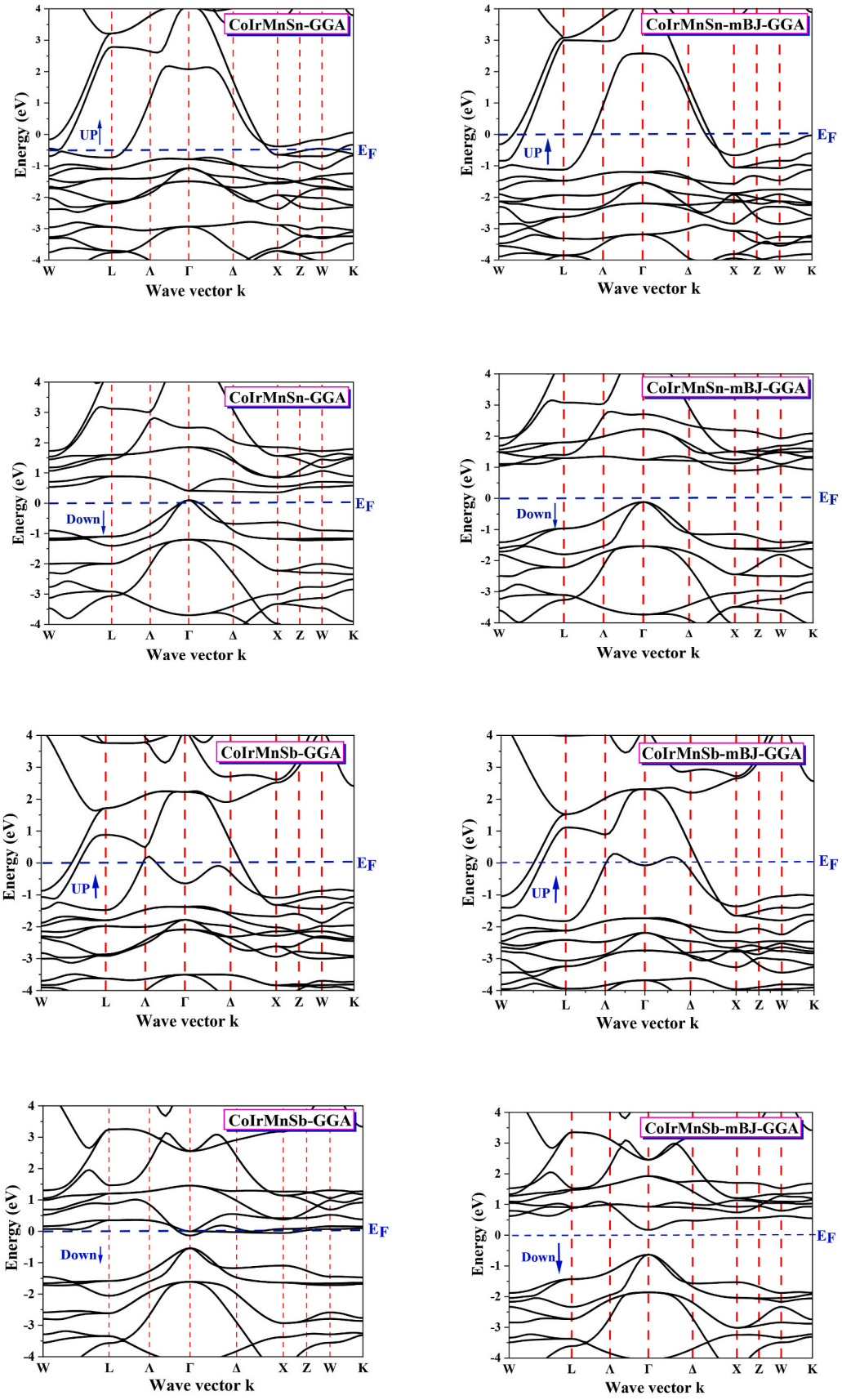

Fig. 4. Energy band structures (↑up and ↓dn) calculated for CoIrMnSn and CoIrMnSb alloys in the most stable Type-III phase with the GGA and mBJ-GGA approximations.

Table 4
Energy gap values calculated by the two GGA and mBJ-GGA approximations for the two quaternary Heusler compounds CoIrMnZ (Z = Sb, Sn).

Compounds	The spins	E_g (eV)	
		GGA	mBJ-GGA
CoIrMnSn-Type III	Up	/	/
	Down	/	1.008
CoIrMnSb-Type III	Up	/	/
	Down	/	0.806

semiconductor-like. CoIrMnSn has a minimum conduction band (CBM) and a maximum valence band (VBM) at high symmetry points *Γ* and *X*, respectively, when minority spins are present. This indicates the presence of an indirect gap, as well as a close proximity between the Fermi energy and the VBM, which corresponds to a *p*-type semiconductor. Conversely, the compound CoIrMnSb exhibits its minimum conduction band (CBM) and maximum valence band (VBM) situated at the high symmetry point Γ. This indicates the presence of a direct gap, as well as a close proximity between the Fermi energy and the CBM, which corresponds to the *n*-type semiconductor. The GGA approximation introduces

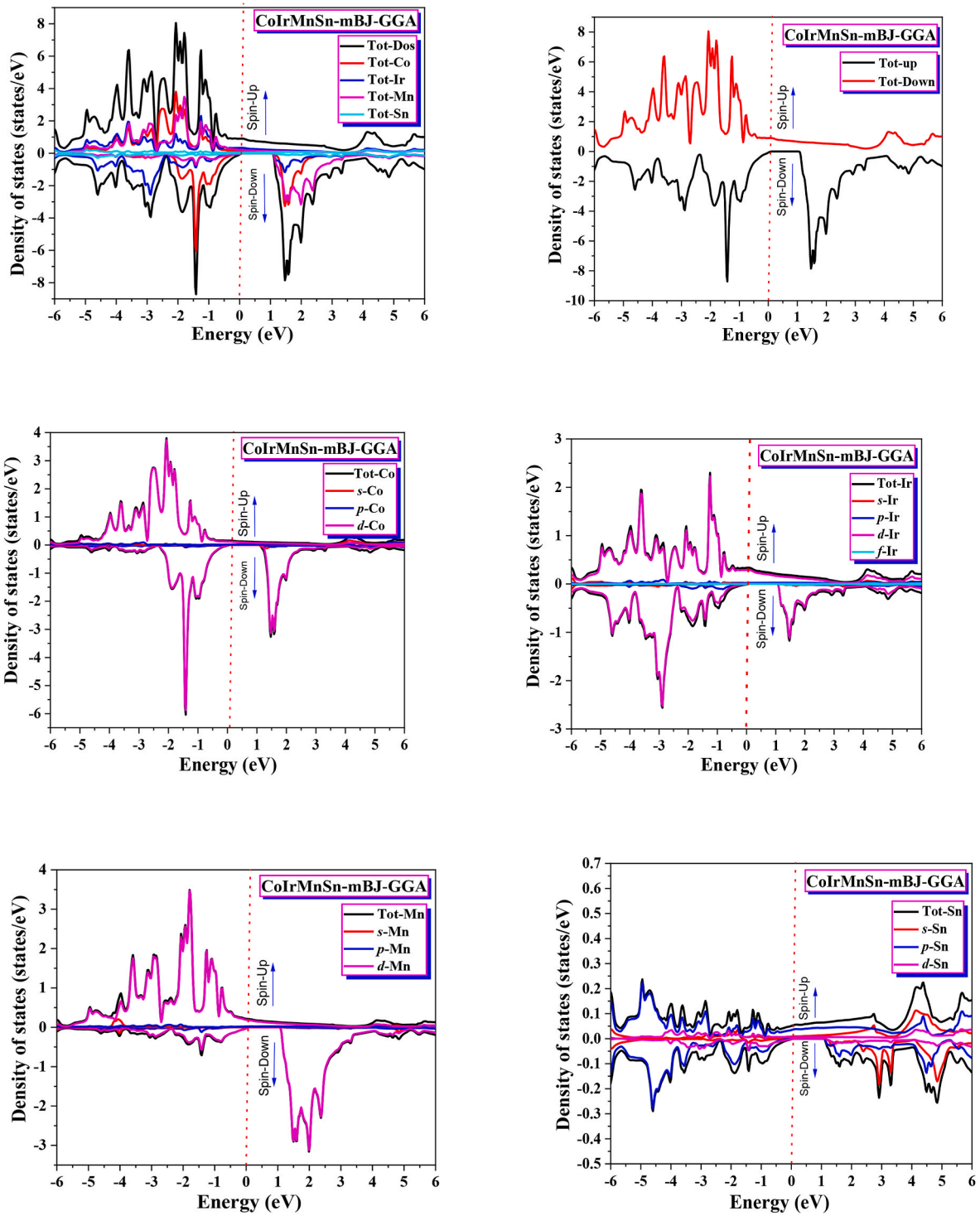

Fig. 5. The total and partial state density of CoIrMnSn and CoIrNSb in Type-III calculated by mBJ-GGA.

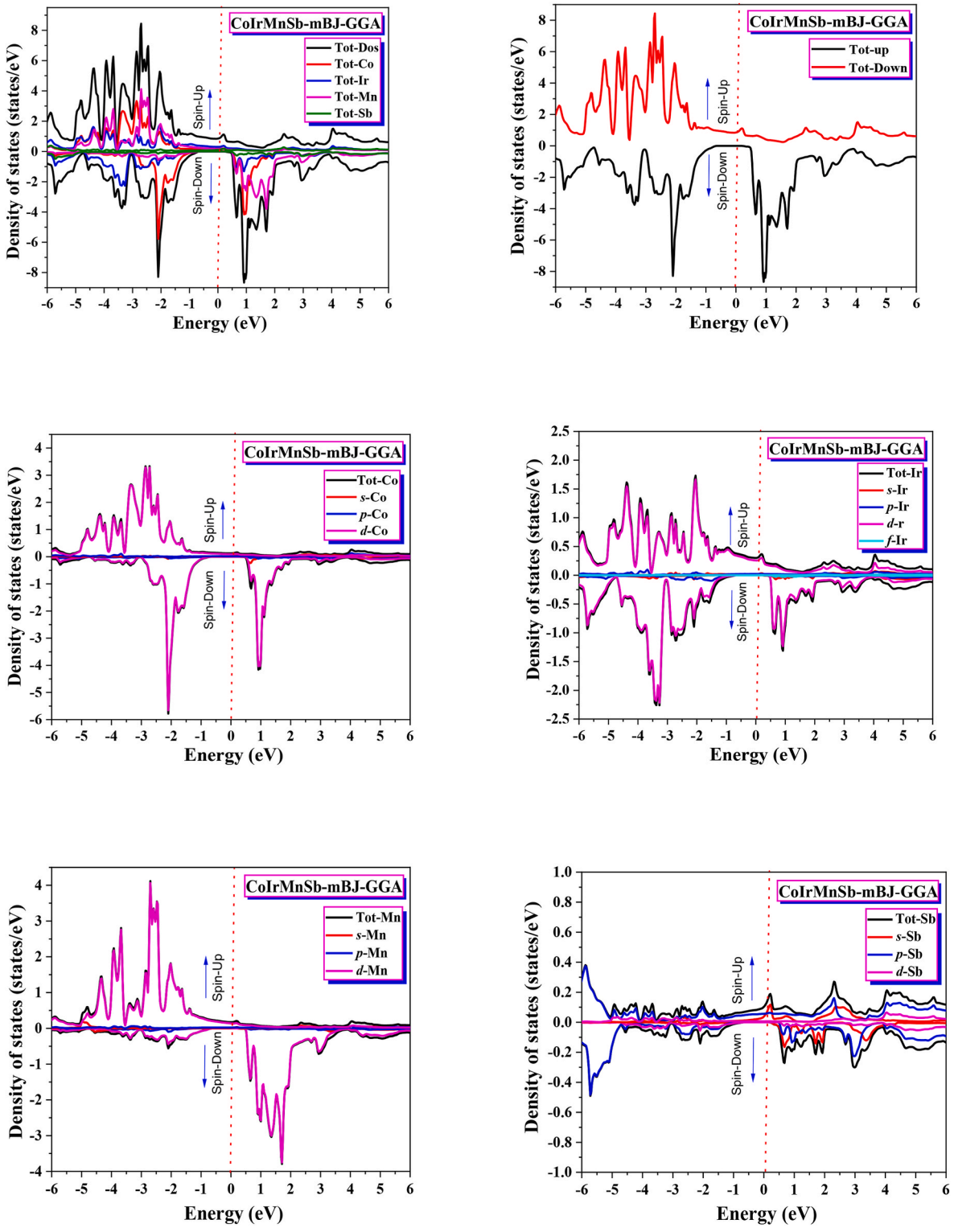

Fig. 5. (*continued*).

a metallic quality to both majority and minority spins due to the fact that the bands associated with up and down spins intersect the *Fermi* energy level. Therefore, when considering the minority spin channel and employing the mBJ-GGA approximation, the CoIrMnSn-Type III and CoIrMnSb-Type III exhibit a band gap of 1.008 eV and 0.806 eV, respectively, as indicated in Table 4. We can infer that the materials under consideration exhibit characteristics consistent with semi-metals based on the mBJ-GGA approximation.

Fig. 5 displays the total and partial state densities of CoIrMnSn and CoIrMnSb, which have been computed using the mBJ-GGA approximation. The depicted curves represent the distribution of electron states as a function of energy. For the CoIrMnZ (Z = Sn, Sb) quaternary compounds, below *Fermi* level, the Co, Mn, and Ir atoms have a majority contribution to the total state density (DOS) of the majority spins due to the *3d*, *3d*, and *5d* layer electrons, respectively, and for the minority spins, the Co and Ir atoms are the majority contributors to the total state

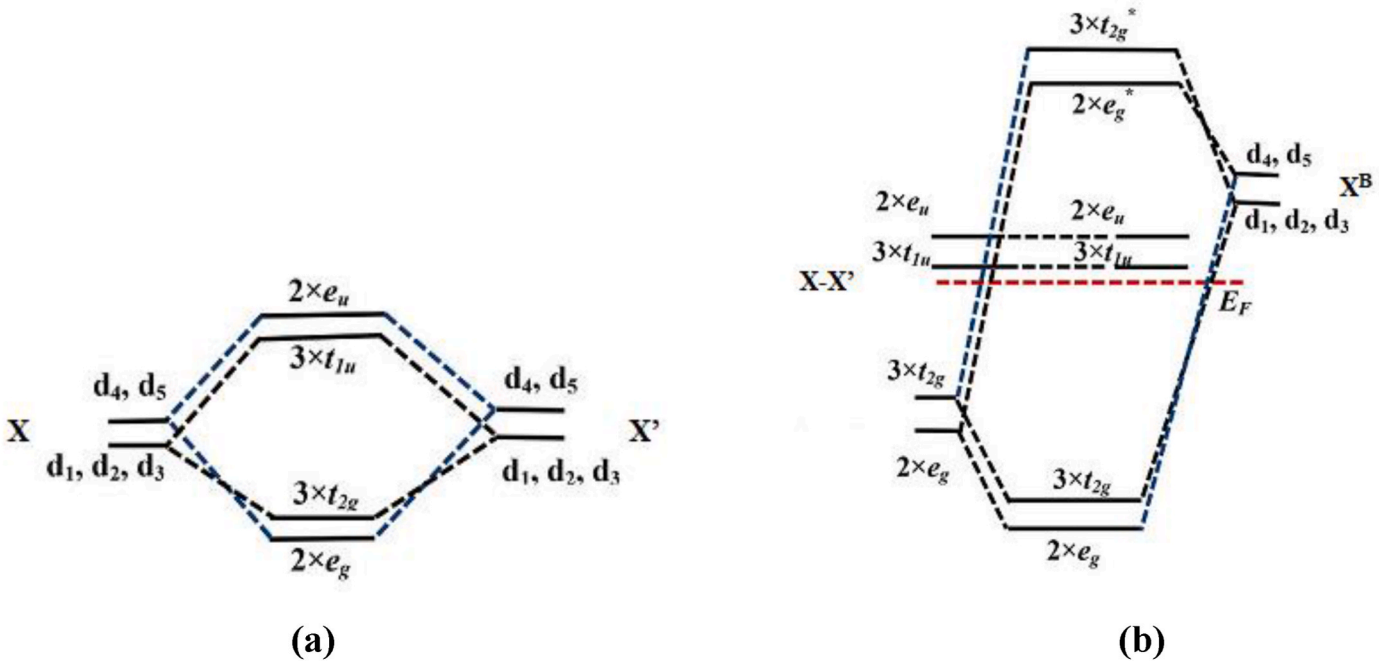

Fig. 6. Possible hybridization schemes for spin-down bands in Type III structures. Figure (a) represents the hybridization between atoms X and X′ at coordinates A and C. Figure (b) shows the hybridization for the compounds following $M_{Tot} = N_v$-24.

density due to the 3*d* and 5*d* layers respectively. With regard to the conductive band, our compounds have a mixed contribution from the orbitals of the atoms X, X′, and Y, and the contribution from the atom Z is neglected.

The Slater-Pauling rule is a notable characteristic of Heusler compounds since it enables the estimation of the total spin magnetic moment, M_{Tot}, based on the total count of valence electrons. This property is regarded as very intriguing. Heusler compounds firmly adhere to the rule of possessing a complete value of the total spin magnetic moment, resulting in the presence of ideal semi-metallic ferromagnetics and semiconductors without a spin gap. The valence electrons of a Heusler compound can exist in either a majority or minority spin state, and this distinction accounts for the observed total spin magnetic moment, as it is determined by the disparity in their quantities. The relative arrangement of the Y atoms with respect to X and X′ in Heusler's quaternary compounds frequently gives rise to an intricate Slater-Pauling rule. All the compounds in our study exhibit adherence to the $M_{Tot} = N_v$-24 principle, where M_{Tot} and N_v denote the total magnetic spin moment and the total number of valence electrons, respectively. The hybridization scheme pertaining to several categories of Heusler alloys is well documented [50,51] and has been frequently employed to elucidate the reported electronic and magnetic characteristics of numerous compounds [52–54].

In Heusler quaternary alloys that adhere to the $M_{Tot} = N_v$-24 principle, the coordination sites A and C in Type III exhibit identical characteristics. Consequently, elements X and X′ undergo initial hybridization, resulting in the formation of double (e_g) and triple (t_{2g}) hybrids. The Y-coordinate transition metal undergoes hybridization with the aforementioned hybrid states, resulting in the formation of five binding states, five anti-binding states, and five non-bonding states. The primary group element (Z) introduces 1 *s* band and three degenerate *p* bands, which possess lower energy levels compared to the *d* bands. These *p* bands contribute to structural stability by reducing the effective concentration of the *d* charge. We are interested in the relative arrangement of the non-binding *d*-hybrids in Heusler quaternary alloys, specifically the three occupied states (t_{1u}) and two unoccupied states (e_u). This arrangement plays a crucial role in determining the energy gap of the minority spin band, as depicted in Fig. 6. In compounds with a Type I crystal structure, the presence of X on site B and Y on site D leads to the formation of octahedral symmetry, resulting in the initial hybridization of these elements. Subsequently, these hybrid states hybridize with X′ on site C, resulting in the formation of hybrid states, as previously explained. In the case of Type I and Type III structures, it is clear that the different hybridization patterns caused by different atoms would always cause the bands to be positioned in different ways. It is important to acknowledge that the crystal's structure remains unchanged when the positions of atoms X and X′, as well as Y and Z, are swapped, owing to the symmetry exhibited by space group 216.

The total magnetic moment (M_{Tot}) of the Heusler compounds CoIrMnSn, and CoIrNSb has been determined to be 2 μ_B, and 1 μ_B, respectively, at a pressure of 0 GPa. The complete magnitude of the magnetic moment aligns with the principles outlined in the Slater-Pauling rule. The equation $M_{Tot} = N_v - 2N_d$ represents the relationship between the total number of valence electrons (N_v) and the total number of spin-down states (N_d) per unit cell. In this context, N_v takes on specific values depending on the compound being considered: 29 for CoIrMnSn, 30 for CoIrNnSb. Additionally, N_d has a constant value of 12. The twelve spin-down states consist of 1 *s* state, three *p* states, and 8 *d* states, specifically the states $2e_g$, $3t_{2g}$, and $3t_{1u}$. At point Γ, the band degeneracy is as follows: one for *s* bands, three for *p* bands, two for *e* bands, and three for *t* bands. The bands *e* and *t* are the result of hybridization between the 3*d* and 5*d* orbitals of the Co, Mn, and Ir atoms for the CoIrMnZ (Z = Sn, Sb) compounds.

The spin-up band structures of the Heusler Quaternary Compounds CoIrMnZ (Z = Sb, Sn) exhibit fully occupied valence bands including *s*, *p*, $2e_g$, $3t_{2g}$, $2e_u$, $3t_{1u}$, and $2e_g$, respectively. The *Fermi* level is established at 0 eV and intersects partially filled $3t_{2g}$ conduction bands, resulting in metallic behaviour along the spin up channel for the two compounds investigated (see Fig. 7). The quaternary compounds' spin-down band structures exhibit fully occupied valence bands, specifically the *s*, *p*, $2e_g$, $3t_{2g}$, and $3t_{1u}$ bands, respectively.

The compounds behave like semiconductors because the *Fermi* level is situated between the fully occupied $3t_{1u}$ valence bands and the unoccupied $2e_u$ conduction bands, as shown in Fig. 7. In order to validate the presence of the energy gap, we conducted calculations to determine the overall density at the *Fermi* level, incorporating spin polarisation as

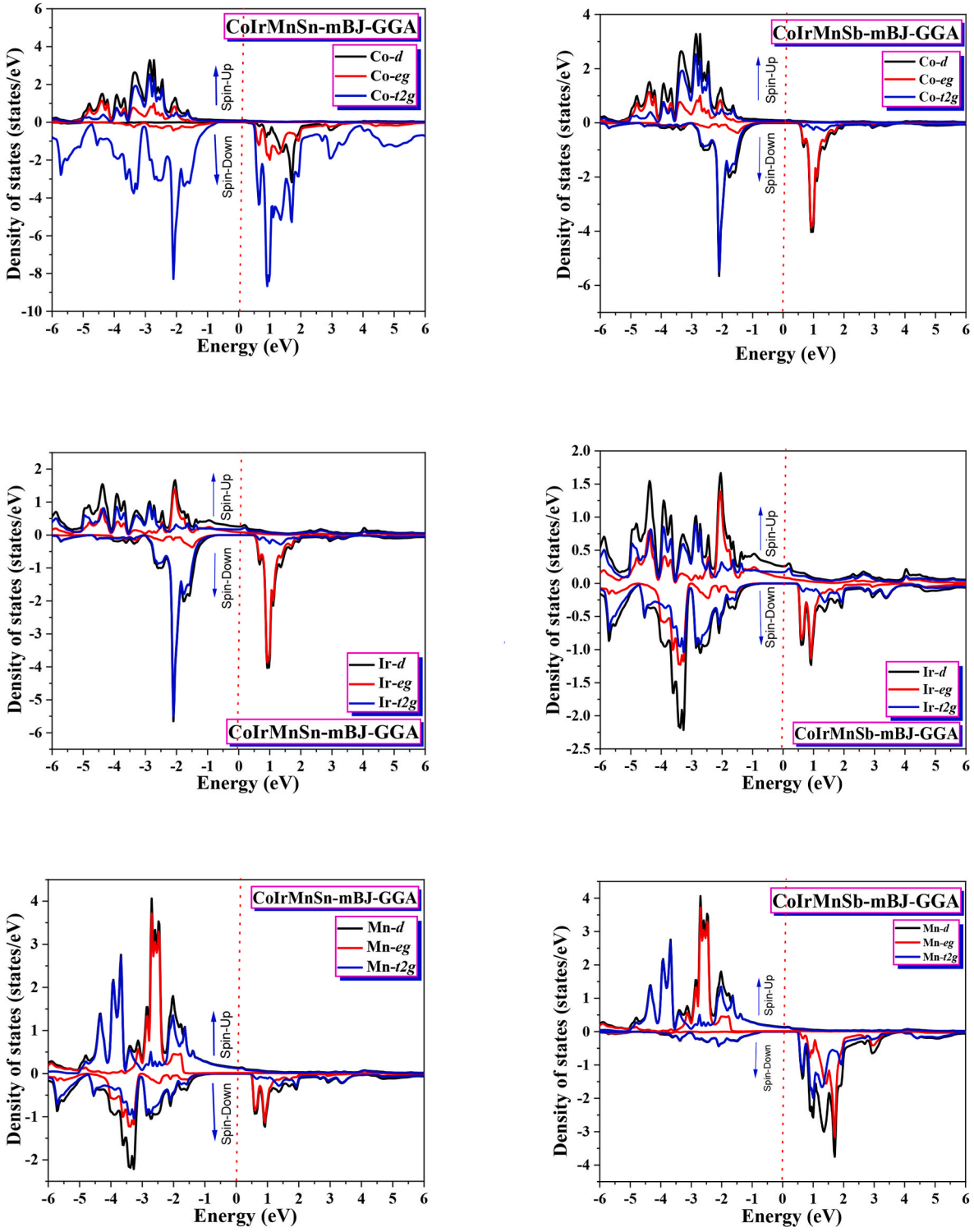

Fig. 7. Partial state densities of the hybrid orbital for majority and minority spin in the compounds CoIrMnSn and CoIrMnSb with mBJ-GGA approximation.

an indicator of the material's characteristics, as described by the subsequent equation:

$$P = \frac{N(E_F)^{\uparrow} - N(E_F)^{\downarrow}}{N(E_F)^{\uparrow} + N(E_F)^{\downarrow}} \tag{7}$$

The Heusler quaternary compounds CoIrMnZ (Z = Sb or Sn) have garnered significant attention in the field of spintronics due to their remarkable electronic spin polarisation properties. We determined the electronic spin polarisation by evaluating the spin polarisation at the *Fermi* energy, using equation (7). This equation is a widely used method for assessing spin polarisation in various materials. The findings presented in Table 5 indicate that the compounds CoIrMnZ (Z = Sb, Sn) exhibit 100 % electron spin polarisation using the mBJ-GGA approximation. The state density analysis shows that the Heusler quaternary compounds CoIrMnZ-Type III (Z = Sb, Sn) have ferromagnetic and semimetallic properties when the mBJ-GGA approximation is used. This finding suggests that these compounds have the potential to become materials suitable for spintronic applications in the future [55]. Based on

Table 5
Total electron density N(E_F) up and down at *Fermi* level with *P* polarisation for Heusler Quaternary Compounds CoIrMnZ (Z = Sb, Sn) and XMnCrZ (X = Ru, Ni and Z = Al, Si) calculated by GGA and mBJ-GGA approximations.

	GGA			mBJ-GGA		
	N(E_F)		*P*	N(E_F)		*P*
	N(E_F)↓	N(E_F)↑		N(E_F) ↓	N(E_F) ↑	
CoIrMnSn-Type III	0.03	0.69	65 %	0	0.70	100 %
CoIrMnSb-Type III	0,3	2,13	73 %	0	11.54	100 %

Table 6
The values of the total and the partial magnetic moment (μ_β) of the compounds CoIrMnSn, CoIrNSb calculated with the approximations GGA and mBJ-GGA.

Compounds	**Parameters (μ_β/*atom*)**	Our calculations		Theoretical calculations [32]
		GGA	mBJ-GGA	
CoIrMnSn-Type III	M(Interstitielle)	−0.00621	−0.21646	/
	M(Co)	1.30103	1.54362	1.38
	M(Ir)	0.31495	0.19219	0.27
	M(Mn)	3.41520	3.53414	3.44
	M(Sn)	−0.02057	−0.04859	−0.03
	M(Tot)	5.00440	5.00489	5.01
CoIrMnSb-Type III	M(Interstitielle)	0.11936	−0.05560	/
	M(Co)	1.51138	1.74074	1.64
	M(Ir)	0.55391	0.50696	0.52
	M(Mn)	3.64959	3.78099	3.68
	M(Sb)	0.04815	0.02703	0.04
	M(Tot)	5.88238	6.00013	6.00

calculations, it can be inferred that these materials possess a high Curie temperature, HM gap, mechanical stability, and complete spin polarisation. These devices, such as magnetic tunnel junctions (MTJs), spin valves, and spin injectors, are appropriate candidates for spintronics applications. Implementing these devices will improve the efficiency of spintronics technology [56–61].

Table 6 displays the calculated local and total magnetic moments for the Heusler quaternary compounds CoIrMnZ (Z = Sb, Sn) using the GGA and mBJ-GGA approximations. The compounds CoIrMnSn and CoIrMnSb exhibit ferromagnetic properties, characterised by an overall magnetic moment of 5 μ_β and 6 μ_β, respectively. The localised magnetic moments of the chromium (Co) and manganese (Mn) atoms primarily influence the overall magnetic moment of the Heusler quaternary compounds CoIrMnSb and CoIrMnSn, with a minor contribution from the iridium atom (Ir). The magnetic moments of tin (Sn) and antimony (Sb) atoms are considered insignificant in relation to the overall magnetic moment.

2.3. Optical properties

Investigating the optical characteristics of solids has emerged as a potent technique for comprehending the electronic attributes of materials. In this analysis, we calculated certain numbers, such as the complex dielectric function [62], which has the following definition:

$$\varepsilon(\omega) = \varepsilon_1(\omega) + i\,\varepsilon_2(\omega) \tag{8}$$

The imaginary part $\varepsilon_2(\omega)$ represents the material's ability to absorb light, while the real part $\varepsilon_1(\omega)$ is associated with the polarisation of the material.

The optical properties, such as the imaginary part $\varepsilon_2(\omega)$ of the dielectric function, were calculated using the mBJ-GGA approximation across an energy range from 0 to 55 eV (Fig. 8 (a)). Assigning values to occupied and unoccupied bands determines the value of the imaginary component of the dielectric function. Following this, the origin of each peak can be determined by examining the consequences of specific electronic transitions that occur between an occupied valence state and a vacant conduction state. From the upper valence bands, the optical spectra transition to the lower conduction bands. The spectra of the imaginary portion of the two half-metals are virtually identical, as shown in Fig. 8(a). The initial critical point in defining the boundary between the valence bands (VB) and the conduction bands (CB) is the optical absorption edge. The information given describes the properties of the material that set the limit for the direct (or indirect) optical change from the upper valence band V1 to the lower conduction band C1. The enumeration of bands occurs in accordance with their relative positioning at the conduction (valence) band's bottom (top). This value is also known as the primary absorption level. For CoIrMnSn, we identified two fundamental absorption peaks, indicated by b1 and b2, located at energies 0.31293 eV and 2.68032 eV, while for the second compound CoIrMnSb, we have two fundamental peaks b1 and b2 in addition to two secondary peaks b3 and b4 located at energies 0.50341 eV, 2.65311 eV, 6.13617 eV, and 8.06818 eV, respectively. In the infrared (visible) region, we find peaks b1 and (b2). The other secondary peaks, b3 and b4, of CoIrMnSb, are located in the ultraviolet region. The electronic transitions in the minority states of b2 and the majority state of b1 are responsible for the observed peaks. The absorption peaks of the dielectric functions of CoIrMnSn and CoIrMnSb transpire at energies of 2.70753 eV and 2.6259 eV, respectively, in the minority state, and 0.31293 eV and 0.50341 eV in the majority state. The optical absorption of the two compounds is of the following order: $\varepsilon_2(\text{CoIrMnSb}) \rangle \varepsilon_2(\text{CoIrMnSn})$. The spectra of both materials transition from CoIrMnSb to CoIrMnSn as their energy decreases. The decrease in band gap value from CoIrMnSn to CoIrMnSb elucidates this phenomenon.

The Kramers-Kronig transformations [63], as shown in Fig. 8(b), derive the real part of the dielectric function from the imaginary part. The static dielectric constants $\varepsilon_1(0)$, calculated from the zero frequency limitations, are displayed in Table 7. The optical spectra shown in this figure display similarities with slight variances, particularly in the placement and intensity of the peaks. Commencing at $\varepsilon_1(0)$, the real part has a positive correlation with the photon energy, as it rises, reaching prominent peaks before eventually reaching zero. Once it surpasses a minimum value, the dispersive component returns to zero. The main peaks obtained from mBJ-GGA calculations are located at 0.01361 eV, and 0.28572 eV, for the compounds CoIrMnSn and CoIrMnSb, respectively. These are located in the infrared spectrum. The real part of the dielectric function becomes zero at energies of 5.1774151 eV and 6.46684285 eV for CoIrMnSn, and CoIrMnSb, respectively, and then we have a slow progression towards zero again around 24.5855 eV and 24.8499 eV for CoIrMnSn and CoIrMnSb, respectively. We observe the highest intensity peak for CoIrMnSb, followed by CoIrMnSn. There is a positive correlation between a smaller energy gap E_g and a higher static value $\varepsilon_1(0)$, which is in line with Penn's model $\varepsilon_1(0) \approx 1 + \left(\frac{\hbar\omega_p}{E_g}\right)^2$ [64], where $\hbar\omega_P$ is the plasma energy. For all compounds, the real part of the dielectric function exhibited a significant anisotropy.

The refractive index governs the extent of light reflection upon reaching the interface. Total internal reflection determines the critical angle in optical devices. The optical characteristics of this substance enhance its significance in a variety of applications. The spectra are depicted in Fig. 8(c), wherein the refractive index generally mirrors the form of the real component, as they are interconnected by the subsequent equation: $n(0) = \sqrt{\varepsilon_1(0)}$. Excitonic transitions in the refractive index spectra result in distinct peaks located precisely at the energy bandgap's boundary. The compounds CoIrMnSn, and CoIrMnSb have zero frequency refractive indices of $n(0) = 6.28433$, and $n(0) = 5.57172$, respectively. Therefore, we can deduce that CoIrMnSn has the highest refractive index value. The refractive index exhibits a positive correlation with frequency up to 1 eV, beyond which it demonstrates a negative correlation up to 23 eV. Additionally, it displays nonlinear characteristics. The calculated static refractive index $n(0)$ is presented alongside $\varepsilon_1(0)$ in the same table. As far as we know, there is no existing empirical

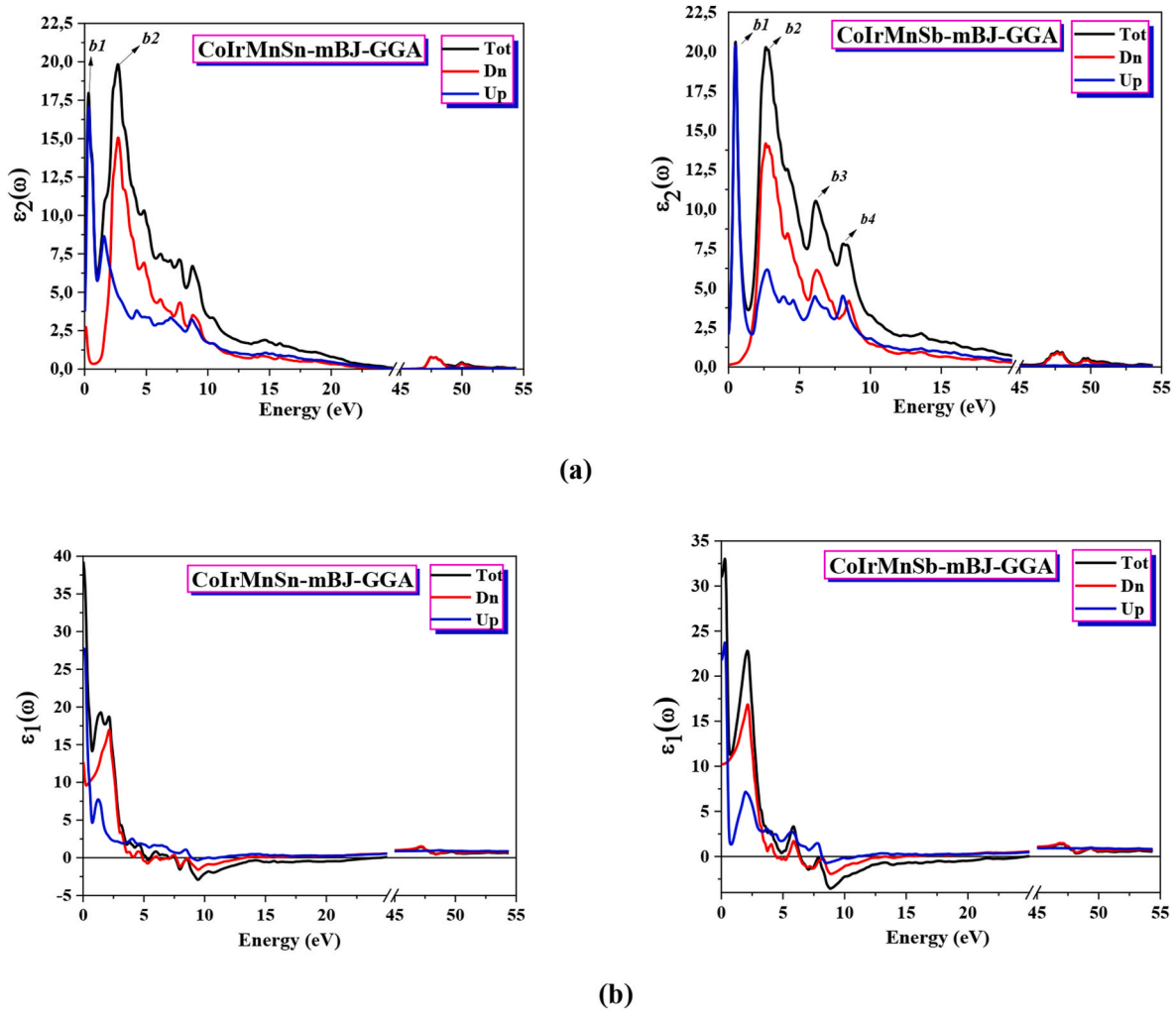

Fig. 8. Variation: of the **(a)** imaginary and **(b)** real part of the dielectric function, **(c)** refractive index, **(d)** extinction coefficient, **(e)** reflectivity, **(f)** absorption coefficient, **(g)** optical conductivity, and **(h)** energy loss function, as a function of photon energy for the compounds CoIrMnSn, and CoIrMnSb with the mBJ-GGA approximation.

or theoretical information that may be used for comparison.

Fig. 8(d) depicts the progression of the extinction coefficient in relation to the photon energy of the compounds under investigation. The spectra exhibit minimal variations in specific aspects. The highest extinction coefficient was seen at an energy level of 2.9180 eV (0.5654 eV) for CoIrMnSn (CoIrMnSb), which is in the visible (infrared) range. This is because of minority (majority) state interband transitions. This value is equal to zero of the real (dispersive) part. Following this maximum, the extinction coefficient immediately declines as the photon energy increases for every compound.

From Fig. 8(e), the reflectivity started at 31.92 % and 27.39 % for the minority spin channel and at 46.50 % and 42 % for the majority states, which leads to a total reflectivity of 52.80 %, and 48.44 % for CoIrMnSn, and CoIrMnSb, respectively. The main peak has an energy of 0.0536 eV, and 24.1016 eV for CoIrMnSn, and CoIrMnSb, respectively. We noticed that the compound CoIrMnSn has the highest reflectivity, followed by CoIrMnSb.

Fig. 8(f) illustrates the relationship between the energy and the absorption coefficient of the Heusler quaternary compounds under investigation. A greater absorption coefficient (10^4 cm^{-1}) is present. For every material: three distinct peaks are identified: b1, b2, and b3. It increases significantly at low energies to reach a peak b1 in the near ultraviolet region, then decreases after another increase to reach a second peak b2, and finally decreases once more after an additional increase to reach a third peak b3. Notably, b2 and b3 are components of the far ultraviolet spectrum. The corresponding (b1, b2, and b3) peaks for CoIrMnSn and CoIrMnSb, are identified at (9.3743 eV, 47.9328 eV, and 50.0009 eV) and (9.9729 eV, 43.0076 eV, and 48.0961 eV), respectively. Interband and intraband transitions between various high symmetries are responsible for the generation of these peaks in the electronic band spectrum. The compounds can subsequently absorb the low-to mid-ultraviolet spectrum efficiently, as illustrated in Fig. 8(f). For CoIrMnSn, the absorption spectra show maximums between 6.0817 and 22.8167 eV, 47.2798 and 48.5043 eV, and 49.6744 and 50.6812 eV. For CoIrMnSb, they are between 5.8368 and 23.9596 eV, 47.0621 and 48.5043 eV, and 49.2934 and 51.3615 eV. CoIrMnSb appears to have the highest absorption coefficient, followed by CoIrMnSn. Due to the fact that these Heusler quaternary materials have a broad absorption band and high absorption intensity, it is possible that they could be utilised in optoelectronic devices.

Optical conductivity $\sigma(\omega)$ is the measure of a material's capacity to transmit light. The relationship between the oscillating electric field $E(\omega)$ and the current density $j(\omega)$ is expressed by the equation $j(\omega) = E(\omega)\sigma(\omega)$, as stated by Ref. [65]. At $\omega \rightarrow 0$, it undergoes a transformation into electrical conductivity. The imaginary component of the dielectric function directly correlates with it [66]. Fig. 8(g) displays an optical

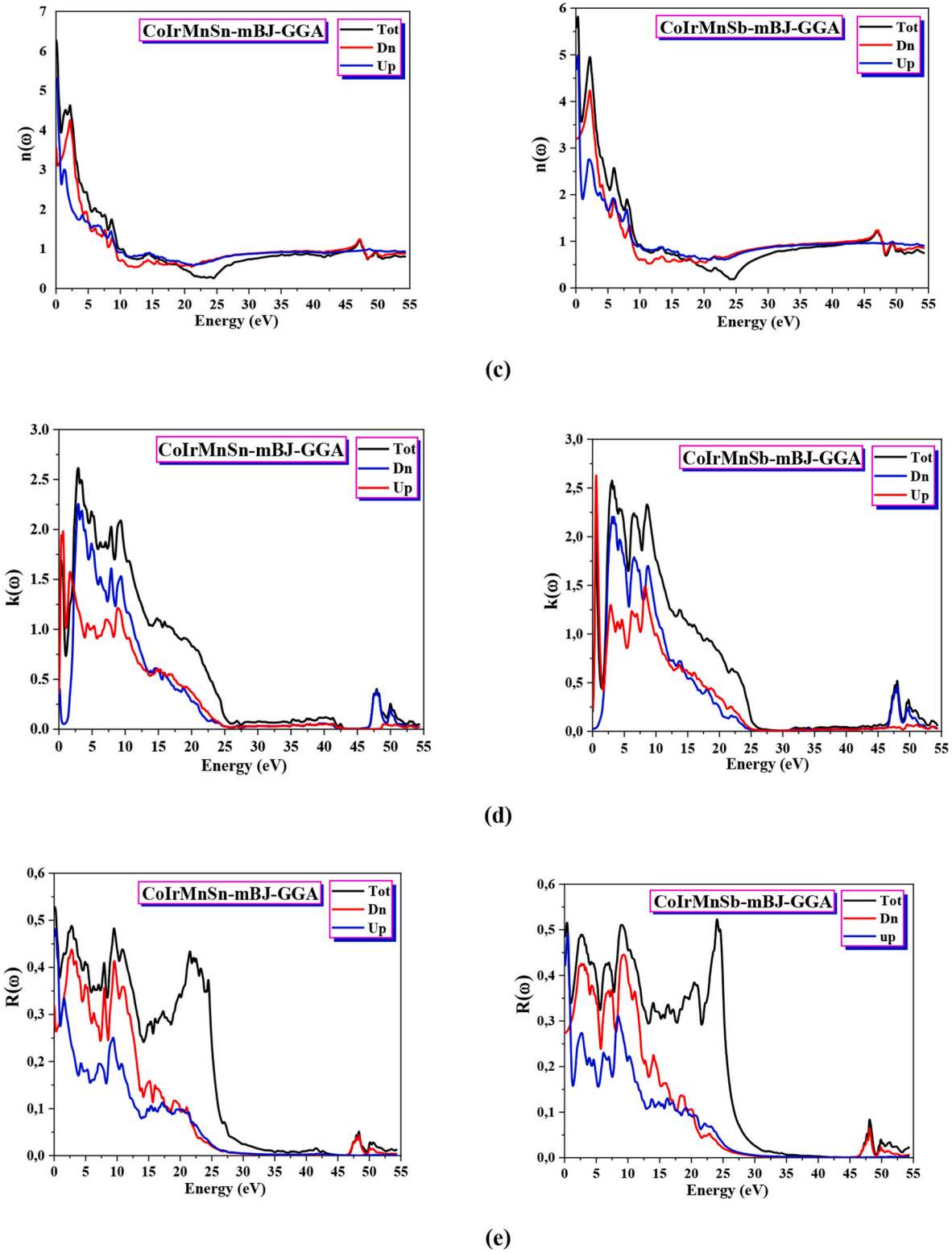

Fig. 8. (*continued*).

conductivity spectrum that has many peaks associated with band transitions. We observe distinct boundaries across the energy ranges of 2.721–11.1430 eV and 47.0893–50.8444 eV for CoIrMnSn, 2.2449–9.5648 eV, and 46.6267–52.2050 eV for CoIrMnSb, all within the ultraviolet spectrum.

The electron energy loss function (EELF) is an essential parameter for understanding the amount of energy lost by fast-moving electrons as they pass through a material. The identified peaks in the L(ω) spectrum are known as Plasmon peaks. As evidenced in Fig. 8(h): The energy loss spectra of CoIrMnSn exhibit noteworthy values within the energy range of 25.42905 eV–22.4358 eV. CoIrMnSb stands out for its substantial energy loss, with an energy range of 23.3609–25.6185 eV. The maximum energy point is 24.8499 eV. The mean value of the plasma frequency ω_p is used to represent the highest point of the energy loss

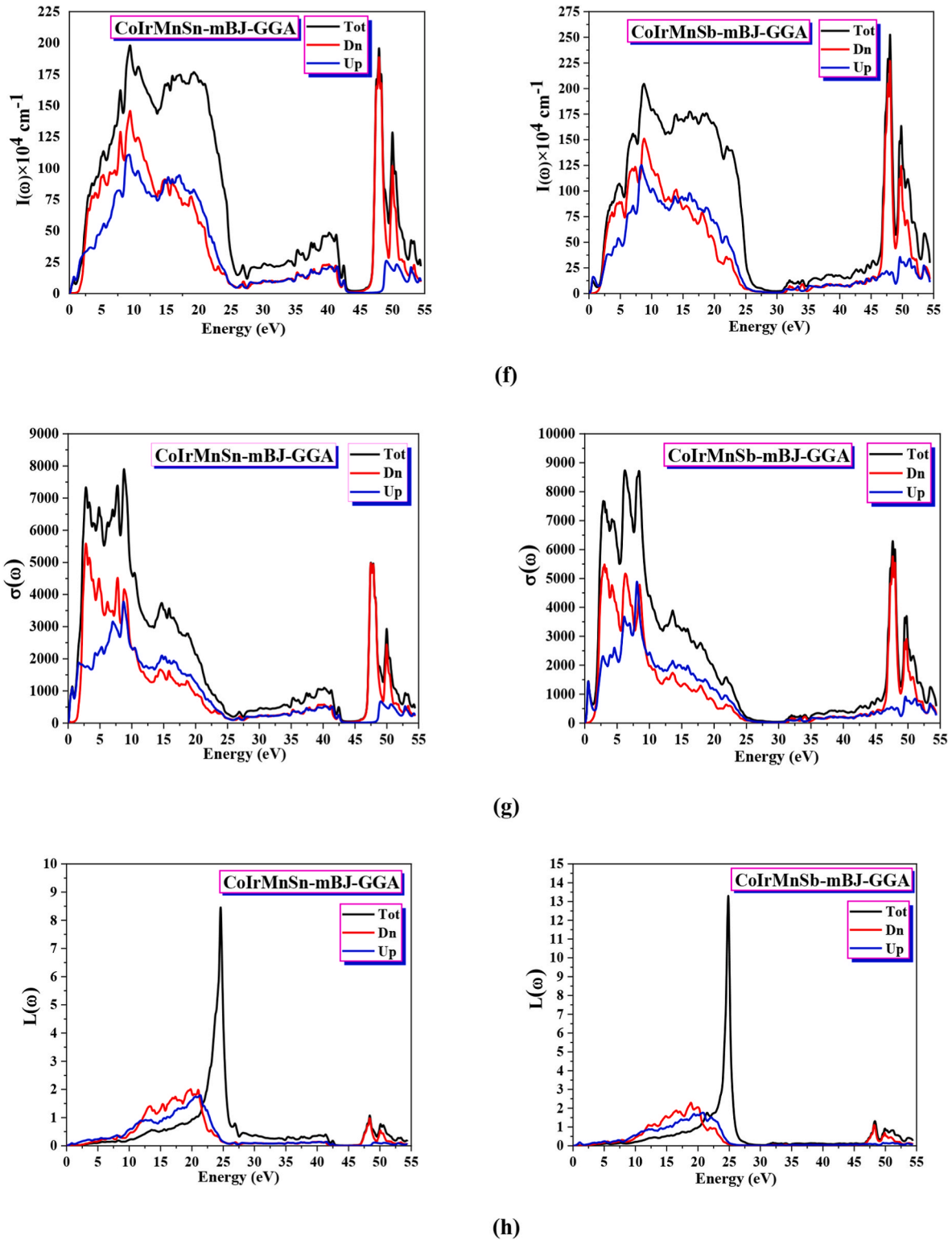

Fig. 8. (*continued*).

function. Therefore, to clarify, the highest plasma energies $\hbar\omega_p$ for CoIrMnSn and CoIrMnSb are 24.5855 eV and 24.8499 eV, respectively. Plasma frequencies for the Heusler quaternary compounds CoIrMnSn, and CoIrMnSb are 3.7445×10^{16} s^{-1}, 3.8437×10^{16} s^{-1}, respectively.

2.4. Thermoelectric properties

The increasing demand for energy has motivated scientists to investigate novel materials and devices that demonstrate exceptional efficiency in the conversion of thermal energy to electrical power. Materials with thermoelectric (TE) properties are potentially applicable in this setting. These compounds have the ability to utilize the Seebeck or Peltier phenomenon, which is useful in the generation of electrical power. As a result, TE materials demonstrate an extensive array of potential applications in energy devices [67,68]. A thermoelectric material that is considered ideal has the following characteristics: a low

Table 7
The values $\varepsilon_1(0)$ of $n(0)$ and calculated for the compounds CoIrMnSn, CoIrMnSb, NiMnCrAl and RuMnCrSi with the GGA, mBJ-GGA approximations.

Compounds	$\varepsilon_1(0)$			$n(0)$		
	Spins	GGA	mBJ-GGA	Spins	GGA	mBJ-GGA
CoIrMnSn-Type III	Up	31.0296	27.5824	Up	5.58628	5.26391
	Down	16.9285	12.7041	Down	4.11848	3.57486
	Total	46.9581	39.2865	Total	0.686747	6.28433
CoIrMnSb-Type III	Up	25.2531	21.7898	Up	5.03172	4.67321
	Down	15.9796	10.2148	Down	4.00001	3.19613
	Total	40.2326	31.0046	Total	6.34966	5.57172

electronic conductivity (σ), a high Seebeck coefficient (S), and a low thermal conductivity (k). Conversely, the thermal conversion capacity (ZT) and the power factor (PF)=$S^2\sigma$ determine the thermal conversion power. Our main goal with this research is to find out different thermoelectric parameters about CoIrMnX (X = Sn, Sb), such as carrier concentration (n), (σ), (k_e), (S), and (ZT). We investigate the properties by applying the semiclassical Boltzmann transport method, BoltzTrap [27]. We also calculate the lattice thermal conductivity (k_L) using Slack's expression [69]. Fig. 9 displays the graphical representation of the parameters in relation to temperature. To guarantee precise convergence, a constant relaxation time assumption of 10^{-14} s was implemented.

The thermoelectric capacity is calculated by working out the capability of the material to generate useable electric energy from waste heat. The figure of merit is $ZT = \frac{\sigma S^2 T}{k_{Tot}}$ where S is the Seebeck coefficient σ is electrical conductivity, T is temperature, and k_{Tot} is the total thermal conductivity. It is possible to calculate a device's total thermal conductivity $k_{Tot} = k_L + k_e$ by adding together its lattice thermal conductivity k_L and electronic thermal conductivity k_e. For a complete picture of how thermal conductivities vary with temperature, look no further than Fig. 9 (a)–(c).

The Slacks equation was used to figure out the lattice thermal conductivity [69,70]:

$$k_L = A\frac{\overline{M}\Theta_D^3\delta}{\gamma^2 Tn^{2/3}} \tag{9}$$

Where A is a physical constant, it may be computed using the following formula:

$$A = \frac{2.43 * 10^{-8}}{1 - \frac{0.514}{\gamma} + \frac{0.228}{\gamma^2}} \tag{10}$$

γ is the Grüneisen parameter, Θ_D is the Debye temperature, n is the number of atoms in the primitive unit cell, $\overline{M}$ is the atoms' average mass in the crystal, and δ^3 is the average volume occupied by one atom of the crystal. The lattice thermal conductivity k_L was determined using *Slack's equation* and *BoltzTrap* code was used to assess the electronic thermal conductivity k_e.

Fig. 9 (a)–(b) illustrate the thermal conductivity components k_L and k_e, which collectively form the total thermal conductivity k_T. We used Slack's model [69,70] to calculate the thermal conductivity (k_L) for the compounds CoIrMnSn and CoIrMnSb over a temperature range of 50–1400 K. Fig. 9 (a) illustrates this. The thermal conductivity values (k_L) of CoIrMnSn (CoIrMnSb) at 300 K and 1000 K are 12.6381 (14.8801) W/mK and 3.1887 (3.8791) W/mK, respectively. At a temperature of 300 K, the Grüneisen parameter (γ) and θ_D for the CoIrMnSn (CoIrMnSb) compounds were ascertained to be 2.435 (2.91799) and 420.73 K (400.32 K), respectively, using the quasi-harmonic Debye estimate technique [71]. The calculated κ_L, as shown in Fig. 9 (a), exhibits a consistently decreasing trend with increasing temperature, primarily attributed to the increased phonon scattering which align with the findings in the research of R. Zosiamliana et al. [72].

Fig. 9 (b) displays the calculated k_e values for the CoIrMnSn and CoIrMnSb compounds. The plot indicates that the temperature directly influences the value of ke for the compounds under study. As the temperature increased from 300 K to 1000 K, the value for CoIrMnSn (CoIrMnSb) significantly increased, rising from 4.3808 (0.3835) W/mK to 26.1557 (16.1624) W/mK.

Fig. 9 (c) demonstrates that the value of k_T decreases when the temperature increases to approximately 400 (550) K for CoIrMnSn (CoIrMnSb) compounds. This observation indicates a significant reduction in phonon-phonon interactions at lower temperatures. The importance of phonon interactions increases with temperature, resulting in a reduction in kT values. The thermal conductivity value of CoIrMnSn compounds at 400 K is approximately 15.8723 W/m.K., whereas for CoIrMnSb compounds at 550 K, it is approximately 10.9730 W/m.K. These values confirm the accuracy of the measurements.

The Seebeck coefficient (S) is an important metric that provides insight into the thermoelectric conversion of a substance. We computed and graphed the temperature-dependent entropy (S) of the studied compounds, as shown in Fig. 9 (d). The picture illustrates the calculated S values for the compound CoIrMnSn, indicating positive values across all temperatures. These findings indicate the existence of charge carriers with p-type conductivity. Therefore, we assume that the holes serve as the primary charge carriers and significantly contribute to the conduction process. The estimated S values for the compound CoIrMnSb indicate positive values across the temperature range of 50 K–200 K, suggesting the presence of p-type charge carriers. Subsequently, the S values exhibit negativity, indicating the presence of n-type conductivity. The conduction process is fundamentally dependent on electrons, which are considered the primary charge carriers. When the temperature of our compound CoIrMnSn (CoIrMnSb) increases from 300 K to 1000 K, the corresponding value of S increases (decreases) from 72.3577 (−115.5206) μV/K to 111.7684 (−163.6565) μV/K.

The notation σ is used to represent the electron conduction mechanism occurring within materials. The energy band theory states that conductors' ample supply of free charges facilitate conduction, while semiconductors require an external energy input to generate charges. The graph in Fig. 9 (e) illustrates the (σ/τ) values of our compounds, which were calculated throughout a temperature range of 50 K–1400 K. The image depicts a direct relationship between temperature and the ratio of (σ/τ). For the compounds CoIrMnSn (CoIrMnSb), the values of (σ/τ) increase from 53.2845×10^{18} (0.6492×10^{18}) (Ω m s)$^{-1}$ at 300 K to 71.1473×10^{18} (17.6604×10^{18}) (Ω m s)$^{-1}$ at 1000 K. So, our materials exhibit a remarkable ability to convert thermal power to electrical power.

A thermoelectric (TE) material that is considered ideal should have a minimal thermal conductivity (k_T) and a high electrical conductivity (σ). The compounds being studied in this research exhibit compliance with the standards for exceptional thermoelectric materials. The assessment of a material's suitability for thermoelectric applications is determined primarily by its figure of merit (ZT) rather than its power factor (PF). Fig. 9 (f) displays the ZT graphs obtained from the computational investigation of our materials. The CoIrMnSn and CoIrMnSb half-Heusler compounds have a significant maximum ZT value of 0.6057 and 0.4853, respectively, at a temperature of 1000 K and 1150 K, respectively. These materials possess sufficient thermoelectric characteristics, making them suitable candidates for thermoelectric devices used to address the energy issue [73].

The aim of the subsequent section of this study is to forecast the parameters of σ/τ, k_e/τ, S, and ZT in response to varying charge transport concentrations spanning from -10×10^{22} cm^3 to -25×10^{22} cm^3 at 300 K, 600 K, and 900 K.

Fig. 10 (a) depicts the correlation between the ratio (σ/τ) and the charge carrier concentration for the CoIrMnSn and CoIrMnSb compounds. An elevation in the density of holes will result in a reduction in the ratio (σ/τ). Graphs of the temperature-dependent function (σ/τ) show that the function (σ) doesn't change with temperature. The

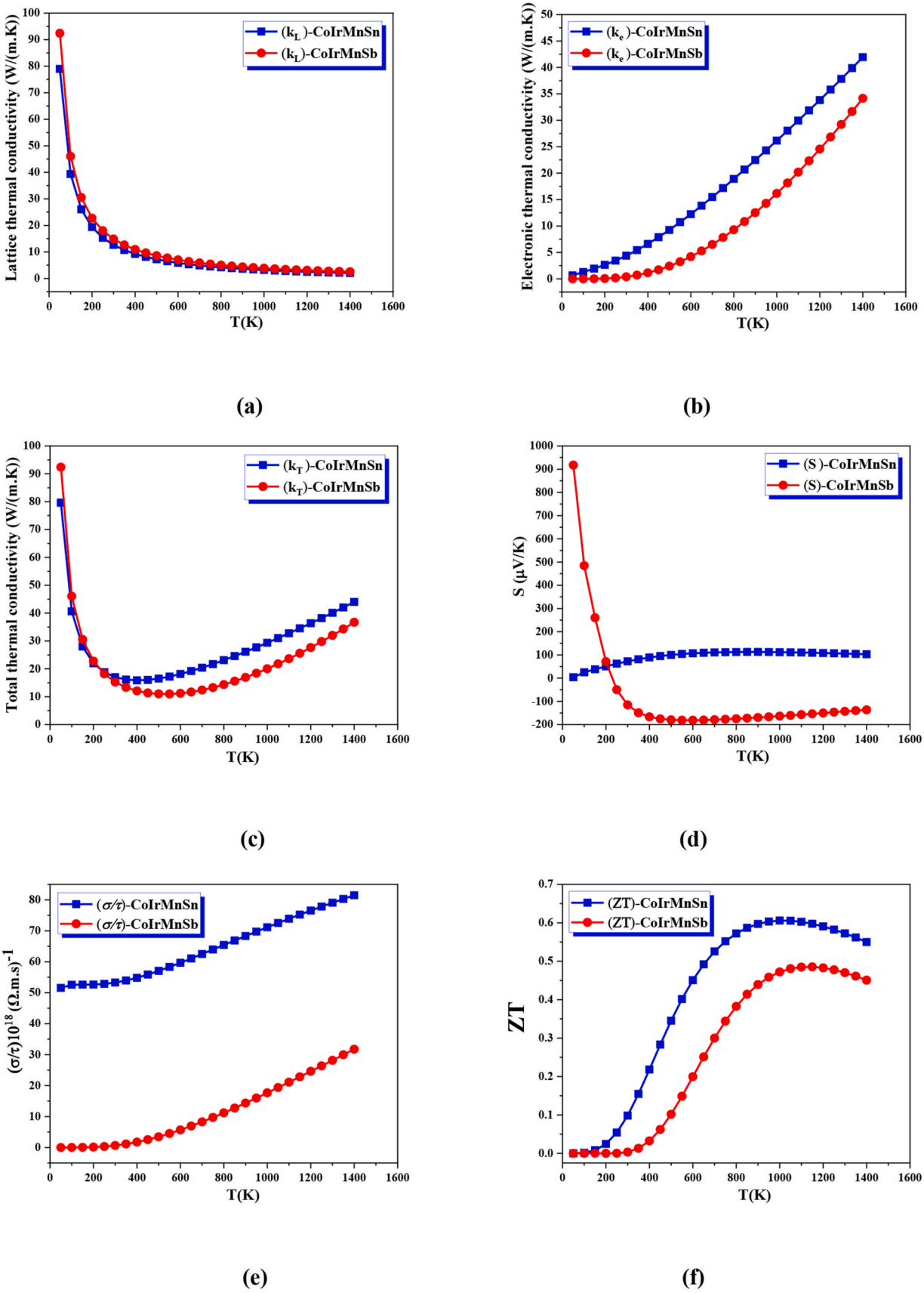

Fig. 9. Temperature sensitivity of: the thermal conductivity of **(a)** the lattice k_L,**(b)** electronics k_e,**(c)** the total k_T, **(d)** Seebeck coefficients S, **(e)** the electrical conductivity via relaxation time (σ/τ),**(f)** the figure of merit ZT of CoIrMnSn and CoIrMnSb compounds based on the mBJ-GGA estimation.

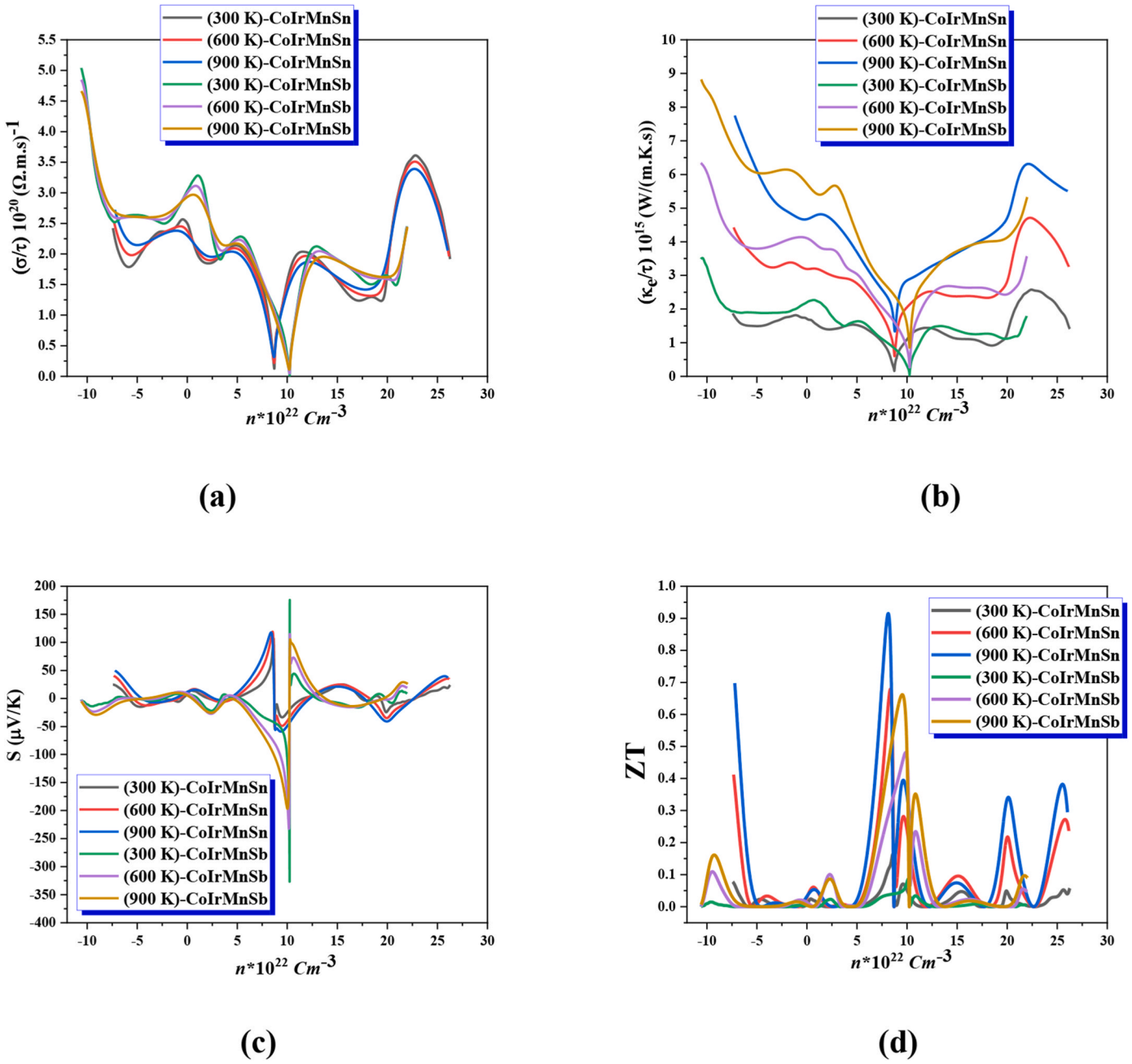

Fig. 10. Forecasted **(a)**, **(b)** conductivities (electrical (σ/τ), electronic thermal (k_e/τ)) as a function of relaxation time, **(c)** coefficient *S* of Seebeck, and **(d)** figure of merit *ZT* via concentrations of charge carriers when T = 300, 600, and 900 K according to the mBJ-GGA approach of CoIrMnSn and CoIrMnSb.

fundamental reason for this phenomenon is that the transport trends, or DOS, within the solid, rather than its temperature, govern the conductivity of the material. For the compound that was studied, CoIrMnSn (CoIrMnSb), there is more delocalization in the conduction band (valence band) compared to the conduction band (valence band) close to the *Fermi* level [74]. This is supported by the observation of a decreased (increased) (σ/τ) ratio in *n*-type compounds in comparison to *p*-type compounds.

Fig. 10 (b) shows the diagrams (k_e/τ) of the compounds CoIrMnSn and CoIrMnSb. Based on the data, observably, the value of (k_e/τ) reduces with the increase in charge carrier concentration caused by the introduction of hole doping. On the other hand, as electron concentration increases, the value of (k_e/τ) will also increase. The corresponding value of (σ) remains constant regardless of temperature; however, the dependency of (k_e) on temperature has been observed. The positive correlation between k_e and temperature explains this phenomenon. Despite this, it seems like σ doesn't.

Temperature primarily affects the Seebeck coefficients (*S*) at large concentrations, which tend to decrease as the temperature rises. Our compounds' narrow bandgaps allow the bipolar effect to influence the susceptibility of their *S* peak. The proportion of carrier mobility exhibited by minority carriers determines the bipolar thermal impact. As the temperature rises, the greatest absolute values of S decrease and converge towards the regions with the highest carrier concentration. As shown in Fig. 10 (c), the amplitudes of the S measurements for *p*-type (*n*-type) CoIrMnSn (CoIrMnSb) compound are greater than those for *n*-type (*p*-type).

The alterations in ZT curves caused by fluctuations in temperature and concentrations of carriers are depicted in Fig. 10 (d). At elevated temperatures, our materials manifest the properties of a thermoelectric

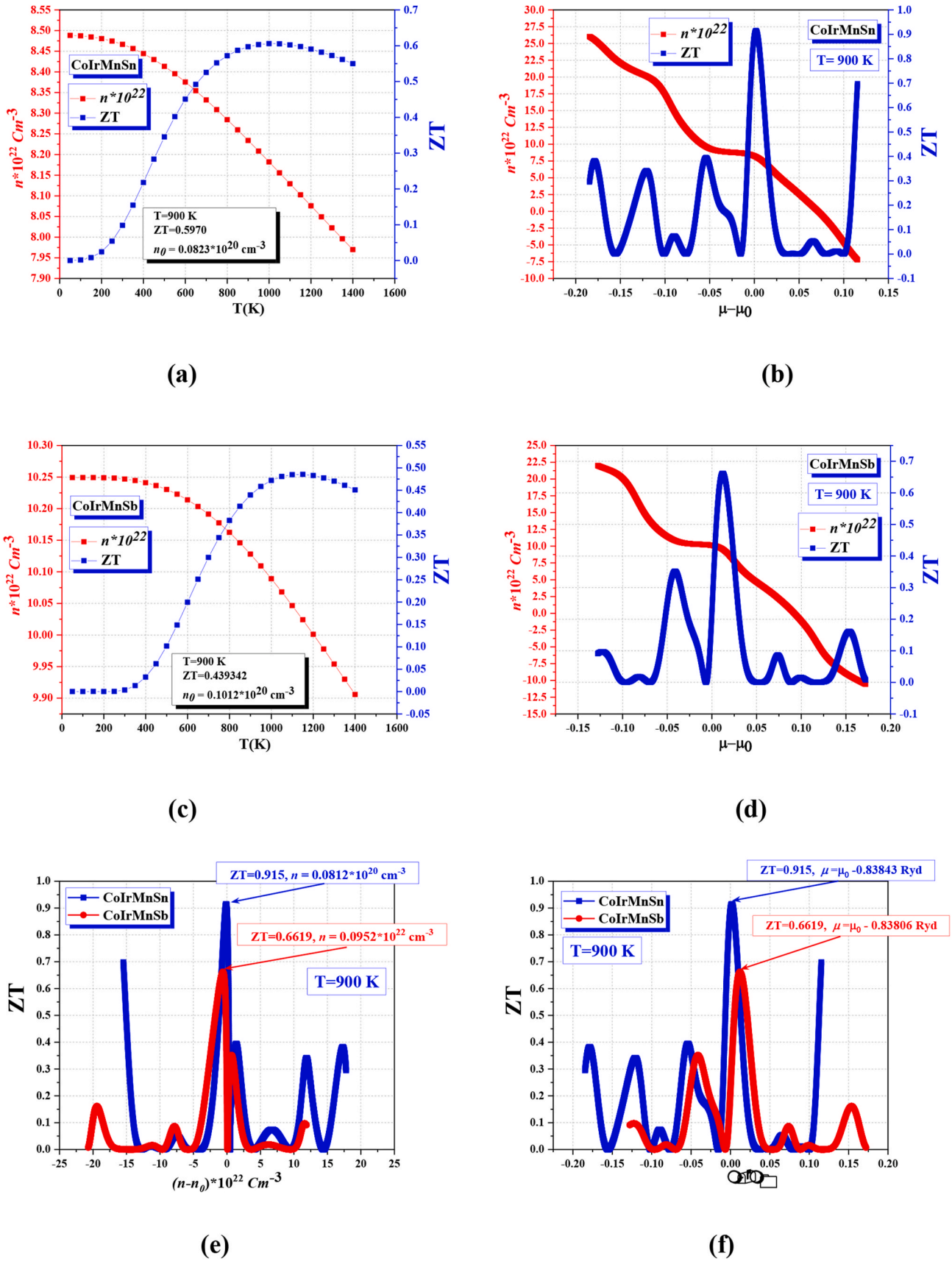

Fig. 11. *ZT* of sHalf-metals CoIrMnSn and CoIrMnSb when T = 900 K vs. **(a), (c)**, and **(e)** concentrations of carrier and temperature, **(b), (d)**, and **(f)** chemical potentials.

half-Heusler, as demonstrated by these figures. *P*-type compounds exhibit considerably higher ZT values in comparison to *n*-type compounds. At a temperature of 900 K, the *p*-type (*n*-type) CoIrMnSn and CoIrMnSb compounds exhibit the greatest ZT values of 0.9149 and 0.6619 (0.6979 and 0.1613), respectively, with corresponding volumes of 0.0091×10^{20} and 0.0952×10^{20} cm^3 (-0.0722×10^{20} and -0.0928 $\times 10^{20}$ cm^3). It can be inferred that the *n*-type and *p*-type of the half-Heusler CoIrMnSn exhibit significant thermoelectric characteristics. The favourable outcomes obtained from these ZT values suggest that the compounds possess significant potential for application as thermoelectric materials. The *n*-type-$Bi_2Al_4Se_8$ material has a thermoelectric figure of merit (ZT) of 0.76 when the carrier concentration (*n*) is -6.448×10^{18} cm^3 [75]. Another *n*-type material, $CuPN_2$, has a ZT of approximately 0.99 with a carrier concentration of -1.7×10^{19} cm^3 [76]. For *p*-type materials, HPN_2 with a carrier concentration of 1.4×10^{19} cm^3 and $LiPN_2$ or $NaPN_2$ with a carrier concentration of 0.4×10^{19} cm^3 have been found to have high ZT values [77]. Additionally, at a temperature of 700 K, the ZT of $CaZn_2Sb_2$ is 0.33 [78]. The *n*-type of LiCrS, LiCrSe, and LiCrTe have ZTs of 0.68, 0.9495, and 0.9507, respectively [79]. The ZT for CoFeTiGe (CoFeCrGe) is 0.25 and 0.404 (0.243 and 0.644) for *n*-type and *p*-type materials, respectively [80]. For the spin-down channel, the highest ZT values are 0.81355, 0.62249, and 1.02846 for RbCrS, RbCrSe, and RbCrTe, respectively [81]. Additionally, when T = 900 K, $ScNbNi_2Sn_2$ achieves a ZT of 0.6391 [82].

2.4.1. How to improve ZT

Fig. 11 (a) and (c) depict the changes in ZT for CoIrMnSn and CoIrMnSb, respectively, over a wide range of temperatures (50 K–1400 K). At 900 K, our CoIrMnSn (CoIrMnSb) compound's thermoelectric figure of merit (ZT) is 0.5970 (0.4393). The obtained outcome is indicative of a carrier concentration (n_0) of 0.0823×10^{20} (or 0.1012×10^{20}) cm^{-3}. The figure of merit (ZT) of half-Heusler CoIrMnSn displays multiple distinct peaks, with three attributed to the *n*-type and two to the *p*-type, as shown in Fig. 11 (b). In the case of the CoIrMnSb compound, the figure of merit (ZT) exhibits two discernible peaks: one associated with the *n*-type and the other with the *p*-type (refer to Fig. 10 (d)). The compound CoIrMnSn (CoIrMnSb) has maximum ZT values of 0.3945 (0.3515) for the *n*-type and 0.9149 (0.6619) for the *p*-type at 900 K, as shown in Fig. 10 (b) and (d). Thus, we can observe discernible distinctions in thermoelectric properties between *p*-type and *n*-type compounds. Therefore, the CoIrMnSn and CoIrMnSb compounds under study exhibit the highest thermoelectric efficacy when compared to other *p*-type compounds. When (μ-$\mu_0 = 0$), it is established that the ZT value for CoIrMnSn is 0.9112. Our findings provide evidence that the thermoelectric properties of our CoIrMnSn compound maintain high efficiency even without doping.

To achieve the maximum attainable ZT value, it is imperative to ascertain the ideal carrier concentration and temperature. We recommend investigating the potential impact of doping concentrations on the figure of merit (ZT) at a temperature of 900 K. The maximal ZT value of CoIrMnSn (CoIrMnSb) is 0.915 (0.6619), as depicted in Fig. 11 (e) and (f). Achieving this value requires reducing the concentration of charge carriers to n = 0.0812×10^{20} (0.0952×10^{20}) cm^{-3} or reducing μ to 0.83843 (0.83806) Ryd. As a result, both materials have promising potential for use in the thermoelectric domain.

3. Conclusion

This study investigated the electronic structure, magnetism, mechanical, optical, and thermoelectric aspects of CoIrMnX (where X = Sn, Sb) using the Wien2k computational code. The current investigation entailed computing the spin-polarised band structure for CoIrMnSn-Type III and CoIrMnSb-Type III, which are quaternary Heusler compounds. The compounds denoted as CoIrMnX (where X = Sn, Sb) demonstrate semi-metallic characteristics as estimated by the mBJ-GGA. This is due to the fact that the majority of spin bands display metallic characteristics by surpassing the Fermi energy level, whereas the minority spin bands have a semiconducting structure. Following the mBJ-GGA approximation and analysis in the minority spin channel, we found that the band gaps of the quaternary Heusler compounds CoIrMnSn and CoIrMnSb are 1.008 eV and 0.806 eV, respectively. The compounds CoIrMnSn and CoIrMnSb exhibit ferromagnetic behavior, as evidenced by their respective total magnetic moments of 5 and 6 μ_β, respectively. This investigation details the optical properties of the quaternary Heusler compounds CoIrMnSn and CoIrMnSb. This study presents and analyses general models of optical parameters, including the real and imaginary components of the dielectric constant, absorption coefficients, and refractive index. The findings suggest that the energy disparities among these parameters are negligible. the values of $n(0)$ and $\varepsilon_1(0)$ indicate an increasing trend from CoIrMnSb to CoIrMnSn. The ultraviolet (UV) spectrum is where the compounds CoIrMnSn and CoIrMnSb exhibit absorption, which makes them advantageous candidates for application in UV photodetectors, UV emitting devices, and power electronic devices. Due to their intrinsic absorption limitations and the presence of the most intensive absorption peaks, this is the case. The maximum ZT value for CoIrMnSn (CoIrMnSb) is 0.915 (0.6619). To achieve this value, it is necessary to either reduce the charge carrier concentration to $n = 0.0812 \times 10^{20}$ (0.0952×10^{20}) cm^{-3} or the μ to 0.83843 (0.83806) Ryd. Substantially examined materials demonstrate considerable potential for application in the field of thermoelectrics.

CRediT authorship contribution statement

T. Ghellab: Writing – review & editing, Writing – original draft, Validation, Methodology, Investigation. **Charifi Z:** Writing – review & editing, Supervision, Methodology, Conceptualization. **H. Baaziz:** Writing – review & editing, Writing – original draft, Validation, Software, Data curation, Conceptualization.

Declaration of competing interest

I have the honor to write to you. I would like to send you our manuscript entitled "**An Optimizing the thermoelectric behavior of novel quaternary CoIrMnX (X=Sn, Sb) alloys through chemical potential or carrier concentration doping .**" *by* **T. Ghellab et al** to publish at your journal*:* **Solid State Communications** *as a regular paper.*

I declare that we have no known competing financial interests or personal relationships that could have appeared to influence the work reported in this paper.

Data availability

Data will be made available on request.

Acknowledgments

The authors (T. Ghellab, Z. Charifi, and H. Baaziz) would like to thank the general directorate for scientific research and technological development for its financial support during the realization of this work.

References

[1] Z. Liu, S. Guo, Y. Wu, J. Mao, Q. Zhu, H. Zhu, Y. Pei, J. Sui, Y. Zhang, Z. Ren, Adv. Funct. Mater. 29 (2019) 1905044.
[2] M. Wolf, R. Hinterding, A. Feldhoff, Entropy 21 (2019) 1058.
[3] A.M. Dehkordi, M. Zebarjadi, J. He, T.M. Tritt, Mater. Sci. Eng., R 97 (2015) 1–22.
[4] M. Manzoor, D. Behera, R. Sharma, M.W. Iqbal, S.K. Mukherjee, R. Khenata, S. Bin-Omran, T. Alshahrani, E. El Shiekh, T. Ouahrani, J. Solid State Chem. (2023) 124188.
[5] J. Yang, G.P. Meisner, L. Chen, Appl. Phys. Lett. 85 (2004) 1140–1142.
[6] Z. Liu, J. Sun, J. Mao, H. Zhu, W. Ren, J. Zhou, Z. Wang, D.J. Singh, J. Sui, C.-W. Chu, Proc. Natl. Acad. Sci. U. S. A. 115 (2018) 5332–5337.
[7] D. Behera, S. Al-Qaisi, M. Manzoor, R. Sharma, V. Srivastava, M. mana Al-Anazy, E. El Shiekh, S.K. Mukherjee, Mater. Sci. Eng., B 297 (2023) 116765.
[8] D. Behera, S.K. Mukherjee, JETP Lett. (2023) 1–14.

[9] C. Zhang, H. Huang, C. Wu, Z. Zhu, Z. He, G. Liu, Front. Phys. 8 (2020) 232.
[10] L. Bainsla, A.I. Mallick, M.M. Raja, A.K. Nigam, B.S.D.C.S. Varaprasad, Y. K. Takahashi, A. Alam, K.G. Suresh, K. Hono, Phys. Rev. B: Condens. Matter Mater. Phys. 91 (2015) 104408.
[11] S. Bahramian, F. Ahmadian, J. Magn. Magn Mater. 424 (2017) 122–129.
[12] Y.J. Zhang, Z.H. Liu, G.T. Li, X.Q. Ma, G.D. Liu, J. Alloys Compd. 616 (2014) 449–453.
[13] S. Idrissi, S. Ziti, H. Labrim, L. Bahmad, Chin. J. Phys. 70 (2021) 312–323.
[14] T. Kaur, J. Singh, M. Goyal, K. Kaur, S.A. Khandy, M.A. Bhat, U.B. Sharopov, S. Dhiman, A.F. Wani, B. Rani, Phys. Scr. 97 (2022) 105706.
[15] R. Haleoot, B. Hamad, J. Phys. Condens. Matter 32 (2019) 75402.
[16] H. Kara, M.U. Kahaly, K. Ozdogan, J. Alloys Compd. 735 (2018) 950–958.
[17] S. Idrissi, H. Labrim, S. Ziti, L. Bahmad, J. Supercond. Novel Magn. 33 (2020) 3087–3095.
[18] J.A. Abraham, R. Sharma, S.A. Dar, S. Chowdhury, Int. J. Energy Res. 46 (2022) 13511–13527.
[19] Y. Gupta, M.M. Sinha, S.S. Verma, J. Solid State Chem. 304 (2021) 122601.
[20] J. Singh, K. Kaur, S.A. Khandy, M. Goyal, S. Dhiman, S.S. Verma, Mater. Today: Proc. 57 (2022) 211–216.
[21] P. Blaha, K. Schwarz, G.K. Madsen, D. Kvasnicka, J. Luitz, wien2k. An Augmented Plane Wave+ Local Orbitals Program for Calculating Crystal Properties, Vienna University of Technology, Vienna, 2001.
[22] J.P. Perdew, K. Burke, M. Ernzerhof, Phys. Rev. Lett. 100 (13) (2008) 136406.
[23] F. Tran, P. Blaha, Phys. Rev. Lett. 102 (2009) 226401.
[24] D.J. Singh, Phys. Rev. B 82 (20) (2010) 205102.
[25] J. Camargo-Martínez, R. Baquero, Phys. Rev. B 86 (19) (2012) 195106.
[26] F. Tran, P. Blaha, Phys. Rev. Lett. 102 (22) (2009) 226401.
[27] G.K.H. Madsen, D.J. Singh, Comput. Phys. Commun. 175 (2006) 67–71.
[28] M. Jamal, M. Bilal, I. Ahmad, S. Jalali-Asadabadi, J. Alloys Compd. 735 (2018) 569–579.
[29] A. Otero-de-la-Roza, V. Luaña, Comput. Phys. Commun. 182 (2011) 1708–1720.
[30] X. Dai, G. Liu, G.H. Fecher, C. Felser, Y. Li, H. Liu, J. Appl. Phys. 105 (2009) 07E901.
[31] V. Alijani, S. Ouardi, G.H. Fecher, J. Winterlik, S.S. Naghavi, X. Kozina, G. Stryganyuk, C. Felser, E. Ikenaga, Y. Yamashita, et al., Phys. Rev. B 84 (2011) 224416.
[32] S. Nepal, R. Dhakal, I. Galanakis, S.M. Winter, R.P. Adhikari, G.C. Kaphle, Phys. Rev. Mater. 6 (2022) 114407.
[33] I. Bensehil, H. Baaziz, T. Ghellab, Z. Charifi Z., A. Kolli, N. Guechi, Phys. Status Solidi B 260 (2023) 2300178, https://doi.org/10.1002/pssb.202300178.
[34] I. Benaisti, N. Guechi, M. Dehbaoui, et al., Eur. Phys. J. B 95 (2022) 109, https://doi.org/10.1140/epjb/s10051-022-00372-3.
[35] I. Waller, Acta Crystallogr. 9 (1956) 837–838.
[36] A. Bouhemadou, R. Khenata, Phys. Lett. 362 (2007) 476–479.
[37] S. Bounab, A. Bentabet, Indian J. Phys. 97 (2023) 1389–1395.
[38] C.M. Kube, AIP Adv. 6 (2016) 95209.
[39] B. Fatima, S.S. Chouhan, N. Acharya, S.P. Sanyal, Intermetallics 53 (2014) 129–139.
[40] J. Haines, J.M. Leger, G. Bocquillon, Annu. Rev. Mater. Res. 31 (2001) 1.
[41] N.A. Teli, M.M.S. Sirajuddeen, Phys. Lett. 384 (2020) 126793.
[42] S.F. Pugh, London, Edinburgh Dublin Philos, Mag. J. Sci. 45 (1954) 823–843.
[43] S.F. Pugh, London, Edinburgh Dublin philos, Mag. J. Sci. 45 (1954) 823–843.
[44] M.E. Eberhart, T.E. Jones, Phys. Rev. B: Condens. Matter Mater. Phys. 86 (2012) 134106.
[45] D. Behera, B. Mohammed, S. Taieb, B. Mokhtar, S. Al-Qaisi, S.K. Mukherjee, Eur. Phys. J. Plus 138 (2023) 520.
[46] M. Manzoor, D. Behera, R. Sharma, M.W. Iqbal, S.K. Mukherjee, R. Khenata, S. S. Alarfaji, H.A. Alzahrani, Mater. Today Commun. 34 (2023) 105053.
[47] P. Ravindran, L. Fast, P.A. Korzhavyi, B. Johansson, J. Appl. Phys. 84 (1998) 4891.
[48] S.I. Ranganathan, M. Ostoja-Starzewski, Phys. Rev. Lett. 101 (2008) 55504.
[49] J.F. Nye, Properties of Crystals, Oxford University Press, New York, 1985.
[50] I. Galanakis, P.H. Dederichs, N. Papanikolaou, Phys. Rev. B 66 (2002) 174429.
[51] K. Ozdogan, E. Şaşıoğlu, I. Galanakis, J. Appl. Phys. 113 (2013) 193903.
[52] R. Dhakal, S. Nepal, I. Galanakis, R.P. Adhikari, G.C. Kaphle, J. Alloys Cmpd, 2021 160500.
[53] R. Dhakal, S. Nepal, R. Ray, R. Paudel, G. Kaphle, J. Magn. Magn Mater. 503 (2020) 166588.
[54] S. Nepal, R. Dhakal, I. Galanakis, Mater. Today Commun. 25 (2020) 101498.
[55] I.I. Mazin, Phys. Rev. Lett. 83 (1999) 1427–1430.
[56] Muhammad Isa Khan, Hafsa Arshad, M. Rizwan, S.S.A. Gillani, M. Zafar, Shabbir Ahmed, M. Shakil, J. Alloys Compd. 819 (2020) 152964, https://doi.org/10.1016/j.jallcom.2019.152964.
[57] M. Shakil, Halima Sadia, Muhammad Isa Khan, S.S.A. Gillani, M. Asghar Gadhi, Imed Boukhris, Phys. B Condens. Matter 625 (2022) 413524, https://doi.org/10.1016/j.physb.2021.413524.
[58] M. Shakil, Halima Sadia, I. Zeba, S.S.A. Gillani, Shabbir Ahmad, M. Zafar, Solid State Commun. 325 (2021) 114157, https://doi.org/10.1016/j.ssc.2020.114157.
[59] M. Zafar, Halima Sadia, M. Rizwan, Hafsa Arshad, Shabbir Ahmad, S.S.A. Gillani, Islah u-din, Cao Chuan Bao, Xiao-Ping Wei, M. Shakil, Chin. J. Phys. 64 (2020) 123–137, https://doi.org/10.1016/j.cjph.2020.01.003.
[60] M. Shakil, Hafsa Arshad, Saba Aziz, S.S.A. Gillani, M. Rizwan, M. Zafar, J. Alloys Compd. 856 (2021) 157370, https://doi.org/10.1016/j.jallcom.2020.157370.
[61] M. Shakil, H. Sadia, S.S.A. Gillani, et al., J Supercond Nov Magn 34 (2021) 3243–3254, https://doi.org/10.1007/s10948-021-06066-8.
[62] N.V. Smith, Phys. Rev. B3 (1971) 1862.
[63] W. Shan, W. Walukiewicz, J.W. Ager III, E.E. Haller, J.F. Geisz, D.J. Friedman, J. M. Olson, S.R. Kurtz, Phys. Rev. Lett. 82 (1999) 1221.
[64] D.R. Penn, Phys. Rev. B 128 (1962) 2093.
[65] J.M. Khoshman, P. Jakkala, D.C. Ingram, M.E. Kordesch, J. NonCryst, Solids 31 (2016) 440.
[66] A. Bakhshayeshi, M. M. Sarmazdeh, R. T. Mendi, A. Boochani: J. Electron. Mater. 1.
[67] H.J. Goldsmid, R.W. Douglas, J. Appl. Phys. 5 (1954) 386.
[68] T.M. Tritt, Rev. Mater. Res. 41 (2011) 433–448.
[69] G.A. Slack, Solid State Phys. 34 (1979) 1.
[70] D.T. Morelli, V. Jovovic, J.P. Heremans, Phys. Rev. Lett. 101 (2008) 035901.
[71] M.A. Blanco, E. Francisco, V. Luania, Comput. Phys. Commun. 158 (2004) 57–72.
[72] R. Zosiamliana, et al., J. Phys. Condens. Matter 36 (2024) 065501.
[73] M. Shakil, H. Arshad, M. Zafar, M. Rizwan, S.S.A. Gillani, S. Ahmed, Mol. Phys. 118 (24) (2020), https://doi.org/10.1080/00268976.2020.1789770.
[74] H. Ma, C.-L. Yang, M.-S. Wang, X.-G. Ma, Y.-G. Yi, J. Phys. D Appl. Phys. 52 (2019) 255501.
[75] T. Ghellab, H. Baaziz, Z. Charifi, M. Telfah, A. Alsaad, A. Telfah, R. Hergenroder, R. Sabirianov, Mater. Sci. Semicond. Process. 141 (2022) 106415.
[76] T. Ghellab, H. Baaziz, Z. Charifi, K. Bouferrache, M.A. Saeed, A. Telfah, Mater. Res. Express 6 (2019) 075906.
[77] T. Ghellab, H. Baaziz, Z. Charifi, K. Bouferrache, Ş. Uğur, G. Uğurand, H. Ünver, Int. J. Mod. Phys. B 33 (2019) 1950234.
[78] I. Mili, H. Latelli, T. Ghellab, Z. Charifi, H. Baaziz, F. Soyalp, Int. J. Mod. Phys. B 35 (7) (2021) 2150100.
[79] A. Telfah, T. Ghellab, H. Baaziz, Z. Charifi, A.M. Alsaad, R. Sabirianov, J. Magn. Magn Mater. 562 (2022) 169822.
[80] Z. Charifi, T. Ghellab, H. Baaziz, F. Soyalp, Int. J. Energy Res. 46 (10) (2022) 13855–13873, https://doi.org/10.1002/er.8104.
[81] T. Ghellab, H. Baaziz, Z. Charifi, H. Latelli, Phys. B Condens. Matter 653 (2023) 414678, https://doi.org/10.1016/j.physb.2023.414678.
[82] H. Mekki, H. Baaziz, Z. Charifi, T. Ghellab, A.E. Genç, Ş. Uğur, G. Uğur, Solid State Commun. 363 (2023) 115103, https://doi.org/10.1016/j.ssc.2023.11.